JOURNAL OF AIRCRAFT
Vol. 43, No. 1, January–February 2006

Small Disturbance Navier–Stokes Method: Efficient Tool for Predicting Unsteady Air Loads

Alexander Pechloff* and Boris Laschka†
Technische Universität München, 85747 Garching, Germany

Regarding industrial aeroelastic applications, the otherwise common yet computationally expensive procedure of time-accurately solving the unsteady Reynolds-averaged Navier–Stokes (RANS) equations is presently not feasible. However, a numerical method based on the small disturbance formulation of these governing equations can provide an efficient means for predicting aerodynamic loading. With this alternative approach the initial unsteady problem is reduced to a formally steady one for the perturbation part under specification of a time law, thus allowing a solution in the frequency domain. A detailed derivation of the small disturbance Navier–Stokes equations on the theoretical basis of the triple decomposition is presented for high-Reynolds-number flow restricted to harmonic behavior. Validation of the resultant numerical method FLM-SD.NS is performed with a transonic test case for each the NACA 64A010 and NLR 7301 airfoil, respectively, undergoing sinusoidal pitch oscillations. Computational results are in good agreement with experimental data, as well as time-accurate RANS solutions provided by the comparative solvers FLM-NS and FLOWer. Reductions in computational time up to an order of magnitude in relation to FLM-NS are observed.

Nomenclature

c_f	=	skin-friction coefficient
c_l	=	lift coefficient
c_m	=	pitching-moment coefficient
c_p	=	pressure coefficient
c_r	=	airfoil chord length
$\check{c}_r$	=	dimensional airfoil chord length, m
$D_{\check{\mu}}$	=	Spalart–Allmaras turbulent destruction term
$\boldsymbol{E}_{v\psi}$	=	generalized viscous flux vector for the ψ direction
$\boldsymbol{E}_{\psi}$	=	generalized convective flux vector for the ψ direction
e	=	specific total energy
$\boldsymbol{F}, \boldsymbol{G}$	=	convective flux vector in ξ, η direction
$\boldsymbol{F}_v, \boldsymbol{G}_v$	=	viscous flux vector in ξ, η direction
$F_{\check{\mu}}$	=	Spalart–Allmaras turbulent first-order diffusion term
$\check{f}$	=	dimensional frequency, Hz
f_{v1}, f_{v2}, f_w	=	Spalart–Allmaras auxiliary functions
H	=	total enthalpy per unit volume, $\rho e + p$
Im	=	imaginary part, normalized with $\hat{\alpha}$
i	=	imaginary unit
J	=	determinant of the coordinate transformation's Jacobian $x_\xi y_\eta - x_\eta y_\xi$
$\bar{\boldsymbol{K}}_{\psi}$	=	generalized mean Jacobian matrix
k	=	angular frequency, $\sqrt{\gamma}\, Ma_\infty k_{\text{red}}$
k_{red}	=	reduced frequency, $2\pi \check{c}_r \check{f}/\check{u}_\infty$
l_{Re_∞}	=	characteristic length used in the formation of Re_∞
Ma_∞	=	freestream Mach number
$P_{\check{\mu}}$	=	Spalart–Allmaras turbulent production term
Pr	=	Prandtl number, 0.72 (air)
Pr_t	=	turbulent Prandtl number, 0.9 (air)
p	=	static pressure
$\boldsymbol{Q}$	=	conservative state vector in the curvilinear coordinate system
$\boldsymbol{q}$	=	conservative state vector in the Cartesian coordinate system
q_x, q_y	=	components of the Cartesian heat-flux vector
Re	=	real part, normalized with $\hat{\alpha}$
Re_∞	=	freestream Reynolds number
S	=	Sutherland constant, $110\,\text{K}/\check{T}_\infty$
T	=	static temperature
$\boldsymbol{T}$	=	Spalart–Allmaras turbulent source-term vector
$T_{2\pi}$	=	period of oscillation
$\check{T}_\infty$	=	dimensional freestream static temperature, K
u, v	=	velocity in x, y directions
$\check{u}_\infty$	=	dimensional freestream velocity, m s^{-1}
x, y	=	Cartesian coordinates
y^+	=	sublayer-scaled distance of the first grid point above a wall boundary
α	=	incidence angle
γ	=	ratio of specific heats, 1.4 (air)
θ_ψ	=	generalized contravariant velocity multiplied by J
μ	=	molecular viscosity
μ_t	=	eddy viscosity
μ_∞	=	freestream molecular viscosity
$\check{\mu}$	=	Spalart–Allmaras conservative working variable
$\check{\nu}$	=	Spalart–Allmaras primitive working variable
ξ, η	=	curvilinear coordinates
Π_x, Π_y	=	Cartesian energy fluxes
ρ	=	density
τ	=	time
τ_{xx}, τ_{yy}, τ_{xy}, τ_{yx}	=	components of the Cartesian shear-stress tensor
$\tau_{\check{\mu}x}$, $\tau_{\check{\mu}y}$	=	Spalart–Allmaras viscous shear-stress equivalent terms
Φ	=	instantaneous arbitrary field quantity
ψ	=	generalized curvilinear coordinate
$\lvert\omega\rvert$	=	magnitude of vorticity
$\lvert\breve{\omega}\rvert$	=	modified magnitude of vorticity
$\langle\ \rangle$	=	phase average
—	=	time average

Superscripts

0	=	zeroth harmonic

Received 1 November 2004; revision received 2 March 2005; accepted for publication 15 March 2005.

*Research Engineer, Aerodynamics Division, Institute for Fluid Mechanics; alexander@flm.mw.tum.de. Member AIAA.

†Professor Emeritus, Aerodynamics Division, Institute for Fluid Mechanics; office@flm.mw.tum.de. Honorary Fellow AIAA.

1	=	first harmonic
-	=	mean/steady-state
~	=	periodic perturbation
′	=	turbulent fluctuation
*	=	linearized in respect to the perturbation
^	=	perturbation amplitude

Introduction

WITHIN the aeroelastic analysis process a thorough investigation of the effects of unsteady air loads on lifting structures demands the broad variation of such parameters as Mach number, Reynolds number, incidence angle, amplitude, frequency, and eigenmode. When employing conventional time-accurate Euler or Reynolds-averaged Navier–Stokes (RANS) methods, computational effort for the necessary permutations becomes prohibitively high. As periodicity of the flow is obtained only after having calculated a number of cycles per case, simulations at low frequencies become especially time consuming. Thus, the aeronautical industry employs these elaborate solvers only for selective evaluation in critical flight envelope regions. The inherent problem of computational cost for the extensive aeroelastic assessment, however, has been dealt with by utilizing methods relying on less complex flow models. Inviscid numerical solutions of the linear potential, transonic small disturbance, or full potential equations are efficiently calculated and in widespread use. In recent years such approaches have been supplemented by the introduction of small disturbance Euler methods, which allow inviscid flow modeling of greater complexity, while retaining an efficient solution process. Originating from the field of turbomachinery, principal investigations based on the small disturbance Euler equations were performed by Hall and Crawley[1] for flutter/forced response in two-dimensional cascade flows. Under the assumption of harmonic motion, a frequency fomulation yields linear variable coefficient equations for the complex amplitude of the field quantities. Consequently, the elimination of the time dependency allows for an efficient numerical integration and supports the customary aeroelastic modal methods. Furthermore, Lindquist and Giles[2] have shown the suitability of the small disturbance Euler equations for providing high-quality resolution of transonic discontinuities.

A successful transfer of this approach to the external flow problem in the field of aircraft aerodynamics was realized at the Aerodynamics Division of the Institute for Fluid Mechanics (Technische Universität München), where the small disturbance Euler solver FLM-SDEu was developed by Kreiselmaier[3] and Kreiselmaier and Laschka.[4] Validation results for select airfoils and wings performing pitching motions in the sub-, trans-, and supersonic flow regime have demonstrated the ability of FLM-SDEu to provide a fast means for accurately predicting unsteady forces. In the continuing process of establishing FLM-SDEu as a common aeroelastic tool, cooperation with the aeronautics industry has resulted in various studies regarding the unsteady air loads associated with a high-performance aircraft delta wing. Specifically, the aerodynamic effects of various eigenmodes,[5,6] of rigid-body motions,[6] as well as flap efficiency with[6] and without external store[7] have been investigated using FLM-SDEu.

Unfortunately, the aforementioned inviscid methods reach their limitation when confronted with flowfields exhibiting significant viscous effects, such as flow separation or shock boundary-layer interaction. As even efficient approaches based on viscous-inviscid coupling possess evident shortcomings in such cases and traditional time-domain solutions of the RANS equations become unwieldly, extension of a small disturbance Euler method to viscous flow becomes a promising alternative. Once again, the development of a numerical solver based on the the small disturbance Navier–Stokes equations was pioneered by the turbomachinery sector, where Clark and Hall[8] initially utilize such a method for investigating stall flutter in two-dimensional cascades and prove its feasibility. Recently, the German Aerospace Center (DLR) has taken up this approach, substituting the original pseudo-time-stepping integration scheme with an iterative solution process based on the generalized minimum residual.[9]

As the application to the field of aircraft aerodynamics becomes reasonable, the small disturbance Navier–Stokes method FLM-SD.NS is developed from the existing inviscid solver FLM-SDEu by supplementing the additional viscous algorithms. Additionally, the treatment of high-Reynolds-number flow requires the incorporation of a turbulence model in appropriate formulation. The present study is restricted to two-dimensional flows.

Theory

Navier–Stokes Equations

Unsteady compressible viscous flow is governed by the Navier–Stokes equations. Accounting for mesh movement, the system of partial differential equations is expressed in nondimensionalized strong conservation form for a body-fitted curvilinear coordinate system:

$$\frac{\partial \boldsymbol{Q}}{\partial \tau} + \frac{\partial \boldsymbol{F}}{\partial \xi} + \frac{\partial \boldsymbol{G}}{\partial \eta} = \frac{\partial \boldsymbol{F}_v}{\partial \xi} + \frac{\partial \boldsymbol{G}_v}{\partial \eta} \tag{1}$$

The curvilinear state vector of conservative variables $\boldsymbol{Q}$ is specified in relationship to its Cartesian counterpart $\boldsymbol{q}$ as

$$\boldsymbol{Q} = J\boldsymbol{q} = J(\rho, \rho u, \rho v, \rho e)^T \tag{2}$$

Density, the velocity components, as well as the specific total energy are identified as the primitive dependent variables composing $\boldsymbol{q}$. The vectors $\boldsymbol{F}$, $\boldsymbol{G}$ represent the convective and $\boldsymbol{F}_v$, $\boldsymbol{G}_v$ the viscous fluxes in ξ and η direction, respectively. For the sake of compactness, the generalized curvilinear coordinate ψ is introduced, allowing both the convective and viscous flux vector to be expressed in a formulation common to each coordinate direction:

$$\boldsymbol{E}_\psi = \begin{pmatrix} \rho\theta_\psi \\ \rho u\theta_\psi + J\psi_x p \\ \rho v\theta_\psi + J\psi_y p \\ H\theta_\psi - J\psi_t p \end{pmatrix} \tag{3}$$

$$\boldsymbol{E}_{v\psi} = \begin{pmatrix} 0 \\ J\psi_x\tau_{xx} + J\psi_y\tau_{yx} \\ J\psi_x\tau_{xy} + J\psi_y\tau_{yy} \\ J\psi_x\Pi_x + J\psi_y\Pi_y \end{pmatrix} \tag{4}$$

By substituting ψ with ξ or η, the convective and viscous fluxes in the individual directions are obtained, that is, $\boldsymbol{F} = \boldsymbol{E}_\xi$, $\boldsymbol{G} = \boldsymbol{E}_\eta$, and $\boldsymbol{F}_v = \boldsymbol{E}_{v\xi}$, $\boldsymbol{G}_v = \boldsymbol{E}_{v\eta}$. In Eq. (3), θ_ψ substitutes for the generalized contravariant velocity multiplied by J:

$$\theta_\psi = J\psi_x u + J\psi_y v + J\psi_t \tag{5}$$

In this context, static pressure is considered as the fifth primitive dependent variable. The components of the Cartesian shear-stress tensor appearing in Eq. (4) are given for a Newtonian fluid under consideration of Stokes hypothesis by

$$\tau_{xx} = \mu\left(\frac{4}{3}\frac{\partial u}{\partial x} - \frac{2}{3}\frac{\partial v}{\partial y}\right), \qquad \tau_{yy} = \mu\left(\frac{4}{3}\frac{\partial v}{\partial y} - \frac{2}{3}\frac{\partial u}{\partial x}\right)$$

$$\tau_{xy} = \tau_{yx} = \mu\left(\frac{\partial u}{\partial y} + \frac{\partial v}{\partial x}\right) \tag{6}$$

Energy fluxes resulting from shear-stress work and heat transfer are represented in Eq. (4) through

$$\Pi_x = u\tau_{xx} + v\tau_{xy} - q_x, \qquad \Pi_y = u\tau_{yx} + v\tau_{yy} - q_y \tag{7}$$

The components of the Cartesian heat-flux vector obey Fourier's law of heat conduction:

$$q_x = -\frac{\gamma}{\gamma - 1}\frac{\mu}{Pr}\frac{\partial T}{\partial x}, \qquad q_y = -\frac{\gamma}{\gamma - 1}\frac{\mu}{Pr}\frac{\partial T}{\partial y} \tag{8}$$

Assuming a calorically perfect gas, connectivity between the static temperature and pressure is achieved through the thermal equation of state $T = p/\rho$. Supplemented by the caloric equation of state and

the definition for e, an additional relationship between the static pressure and the conservative variables is derived:

$$p = (\gamma - 1)\left[\rho e - \frac{(\rho u)^2 + (\rho v)^2}{2\rho}\right] \tag{9}$$

Final closure of the equation system is provided through Sutherland's law for the molecular viscosity, formulated in respect to aerodynamic flows as

$$\mu = \mu_\infty T^{\frac{3}{2}}[(1+S)/(T+S)]$$

$$\text{with} \qquad \mu_\infty = \sqrt{\gamma}(Ma_\infty/Re_\infty)l_{Re_\infty} \tag{10}$$

Compressible similarity to real flow conditions is realized per initialization of the freestream velocity with $u_\infty = \sqrt{\gamma} Ma_\infty$. The freestream Mach and Reynolds number as well as the characteristic length used in the formation of Re_∞ determine the freestream molecular viscosity. Consequently, adjustment of μ_∞ through these parameters allows for viscous similarity. Nondimensionalization has been realized in respect to dimensional freestream density, pressure, and temperature, as well as a dimensional reference length.

In consideration of a finite volume approach for discretizing the Navier–Stokes equations on a structured grid, J appearing in Eq. (2) represents the volume of an individual cell, whereas the generalized metric terms $J\psi_x$ and $J\psi_y$ in Eqs. (3–5) are the Cartesian components of the cell face normal vector for the ψ direction. Additionally, $J\psi_t$ gives the time rate of change resulting from cell face movement for this vector. Specific definition of the metric terms is provided in Ref. 4. Velocity and temperature gradients appearing in Eqs. (6) and (8), respectively, are not subjected to the curvilinear transformation, as a direct evaluation of these terms in the Cartesian coordinate system is numerically feasible.

Derivation of the Time-Linearized Perturbed Flow Governing Equations

Triple Decomposition

Considering the periodic oscillation of an aerodynamic body under steady freestream conditions, the imposition of an organized unsteadiness onto the viscous flowfield can be observed. In regard to the numerical simulation of this problem, the disturbance is mathematically introduced into the instantaneous Navier–Stokes equations (1) by way of the metric terms. Embedded in a computational grid, the body's movement corresponds to a dislocation of its discretized boundary, subsequently deforming the initial mesh. Therefore, it becomes possible to separate the motion of the spatial coordinate for each individual grid point into a steady mean and periodically perturbed component:

$$x(\xi,\eta,\tau) := \bar{x}(\xi,\eta) + \tilde{x}(\xi,\eta,\tau)$$

$$y(\xi,\eta,\tau) := \bar{y}(\xi,\eta) + \tilde{y}(\xi,\eta,\tau) \tag{11}$$

As J and the generalized metric terms $J\psi_{x,y,t}$ are directly calculated from the coordinates, they can be reformulated in similar manner as

$$J = \bar{J} + \tilde{J}, \qquad J\psi_{x,y,t} = \overline{J\psi}_{x,y,t} + \widetilde{J\psi}_{x,y,t} \tag{12}$$

Because the disturbance is externally imposed, the frequency of the unsteady turbulent flow's underlying organized oscillation is known. Postulating the negligibility of higher harmonics in the response, a triple decomposition of the flow development as suggested by Laschka[10] becomes feasible. An arbitrary instantaneous field quantity Φ is separated into a steady mean component $\bar{\Phi}$, a periodic perturbation $\tilde{\Phi}$, and a turbulent fluctuation Φ':

$$\Phi(\xi,\eta,\tau) := \langle\Phi(\xi,\eta,\tau)\rangle + \Phi'(\xi,\eta,\tau)$$

$$= \bar{\Phi}(\xi,\eta) + \tilde{\Phi}(\xi,\eta,\tau) + \Phi'(\xi,\eta,\tau) \tag{13}$$

After substituting each individual primitive variable in the instantaneous Navier–Stokes equations (1) with their equivalent decomposed quantity according to Eq. (13), disjoined application of the phase average

$$\langle\Phi(\xi,\eta,\tau)\rangle := \lim_{N\to\infty}\frac{1}{N}\sum_{n=1}^{N}\Phi(\xi,\eta,\tau + n\cdot T_{2\pi}) \tag{14}$$

and the time average

$$\bar{\Phi}(\xi,\eta) := \frac{1}{T_{2\pi}}\int_{\tau}^{\tau+T_{2\pi}}\Phi(\xi,\eta,\underline{\tau})\,\mathrm{d}\underline{\tau} \tag{15}$$

yields two distinct sets of equations, respectively, governing unsteady and steady mean flow. In both cases the existent turbulent fluctuations are exclusively composited into averaged correlation terms, the necessary mathematical identities for this process having been provided by Telionis.[11] With the emergence of these turbulent correlations, additional unknowns are introduced into the system, presenting a problem of closure that will require further handling. By subtracting the time-averaged equation system from the phase-averaged one, the governing equations for the periodic perturbed flow are obtained, or as formulated symbolically with the arbitrary flow quantity:

$$\tilde{\Phi}(\xi,\eta,\tau) = \langle\Phi(\xi,\eta,\tau)\rangle - \bar{\Phi}(\xi,\eta) \tag{16}$$

Treatment of Higher-Order Perturbation Terms and Turbulent Correlations

To demonstrate the triple decomposition process, the convective flux in ξ direction $\boldsymbol{F} = \boldsymbol{E}_\xi$ is selected. Reformulating the vector's second component F_2 as

$$F_2 = J\xi_t(\rho u) + J\xi_x(\rho u^2 + p) + J\xi_y(\rho u v)$$

$$= F_{20} + F_{21} + F_{22} \tag{17}$$

the term F_{21}, representing the transformed momentum in Cartesian x-direction, is chosen for the specific analysis. Decomposing the metric and the primitive quantities constituting F_{21} in accordance with Eqs. (12) and (13), while subsequently applying the phase average Eq. (14), yields

$$\langle F_{21}\rangle = (\overline{J\xi}_x + \widetilde{J\xi}_x)(\bar{\rho}\bar{u}^2 + 2\bar{\rho}\bar{u}\tilde{u} + 2\tilde{\rho}\bar{u}\bar{u} + \tilde{\rho}\bar{u}^2$$

$$+ \bar{\rho}\tilde{u}^2 + \tilde{\rho}\tilde{u}^2 + \langle\langle\rho\rangle u'u'\rangle + \langle p\rangle) \tag{18}$$

In obtaining Eq. (18), the following considerations have been made: First, the density fluctuation has been omitted, as for nonhypersonic freestream Mach numbers and insignificant heat transfer the turbulence structure is similar to that of incompressible flows.[12] Second, simple mathematical identities[11] applied after the averaging process allow for the elimination of many correlation products between the mean, perturbed, and turbulent quantities. Consequently, the influence of turbulence on the momentum is reduced to the single remaining averaged term $\langle\langle\rho\rangle u'u'\rangle$ identified as a component of the unsteady Reynolds-stress tensor.

Under the assumption of small disturbances, that is, the degree of unsteadiness imposed onto the flow leads to only minor variations of the mean-state, higher-order perturbation terms appearing in Eq. (18) are deemed negligible. In this regard, terms composited through multiple perturbed primitive quantities, for example, $\overline{J\xi}_x 2\tilde{\rho}\tilde{u}\tilde{u}$, as well as terms combining a perturbed metric with a perturbed primitive quantity, for example, $\widetilde{J\xi}_x\tilde{\rho}\tilde{u}^2$, are disregarded. This process marks a linearization in respect to the time-dependent quantities, indicated through an additional * when rewriting $\langle F_{21}\rangle$:

$$\langle F_{21}\rangle^* = \overline{J\xi}_x(\bar{\rho}\bar{u}^2 + 2\bar{\rho}\bar{u}\tilde{u} + \tilde{\rho}\bar{u}^2 + \langle\langle\rho\rangle u'u'\rangle + \langle p\rangle^*)$$

$$+ \widetilde{J\xi}^*_x(\bar{\rho}\bar{u}^2 + \overline{\langle\rho\rangle u'u'} + \bar{p}^*) \tag{19}$$

Likewise, succesive deomposition, time averaging with Eq. (15) and linearization yields the steady mean part of term F_{21}:

$$\bar{F}^*_{21} = \overline{J\xi}_x(\bar{\rho}\bar{u}^2 + \overline{\langle\rho\rangle u'u'} + \bar{p}^*) \tag{20}$$

In analogy $\overline{\langle\rho\rangle u'u'}$ is identified as a steady component of the Reynolds-stress tensor. Furthermore, emerging linearized phase and time averages of the static pressure $\langle p\rangle^*$ and $\bar{p}^*$, respectively, constitute additional unknowns. By subtracting Eq. (20) from Eq. (19) as per Eq. (16), the sought-after linearized perturbation of term F_{21} is obtained to

$$\tilde{F}^*_{21} = \langle F_{21}\rangle^* - \bar{F}^*_{21} = \overline{J\xi}_x(2\bar{\rho}\bar{u}\tilde{u} + \tilde{\rho}\bar{u}^2 + \tilde{p}^*) + \widetilde{J\xi}^*_x(\bar{\rho}\bar{u}^2 + \bar{p}^*) + \overline{J\xi}_x\widetilde{\langle\rho\rangle u'u'} + \widetilde{J\xi}^*_x\overline{\langle\rho\rangle u'u'} \tag{21}$$

with $\tilde{p}^* = \langle p\rangle^* - \bar{p}^*$ being the equivalent formulation for the static pressure. The periodic perturbation of the Reynolds-stress component is incorporated into Eq. (21) through

$$\widetilde{\langle\rho\rangle u'u'} := \langle\langle\rho\rangle u'u'\rangle - \overline{\langle\rho\rangle u'u'} \tag{22}$$

as defined by Acharaya[13] and Norris.[14]

Localizing the viscous flux vector term corresponding to F_{21} in

$$F_{v2} = J\xi_x\tau_{xx} + J\xi_y\tau_{yx} = F_{v21} + F_{v22} \tag{23}$$

as F_{v21}, subsequent application of the triple decomposition, and linearization results in

$$\tilde{F}^*_{v21} = \langle F_{v21}\rangle^* - \bar{F}^*_{v21} = \overline{J\xi}_x\tilde{\tau}^*_{xx} + \widetilde{J\xi}^*_x\bar{\tau}^*_{xx} \tag{24}$$

for the perturbation part. Through basic mathematical manipulation of the emerging perturbed flow governing equations, the Reynolds-stress terms isolated in Eq. (21) are extracted and introduced into Eq. (24). Alignment with the corresponding shear-stress terms yields

$$\begin{aligned}\tilde{F}^*_{v21} &= \overline{J\xi}_x\left(\tilde{\tau}^*_{xx} - \widetilde{\langle\rho\rangle u'u'}\right) + \widetilde{J\xi}^*_x\left(\bar{\tau}^*_{xx} - \overline{\langle\rho\rangle u'u'}\right)\\ &= \overline{J\xi}_x\tilde{\tau}^*_{\mathrm{tot},xx} + \widetilde{J\xi}^*_x\bar{\tau}^*_{\mathrm{tot},xx}\end{aligned} \tag{25}$$

with $\tilde{\tau}^*_{\mathrm{tot},xx}$ and $\bar{\tau}^*_{\mathrm{tot},xx}$ representing the composited linearized perturbed and mean total shear stress, respectively. Extending Boussinesq's assumption to the perturbed flow analysis, the contribution of the Reynolds stress to the total shear stress is approximated through the perturbed and mean velocity gradients in conjunction with a decomposed eddy viscosity. The perturbed component being expressed as

$$\tilde{\tau}^*_{\mathrm{tot},xx} = (\bar{\mu} + \bar{\mu}_t)\left(\frac{4}{3}\frac{\partial\tilde{u}}{\partial x} - \frac{2}{3}\frac{\partial\tilde{v}}{\partial y}\right) + (\tilde{\mu}^* + \tilde{\mu}^*_t)\left(\frac{4}{3}\frac{\partial\bar{u}}{\partial x} - \frac{2}{3}\frac{\partial\bar{v}}{\partial y}\right) \tag{26}$$

while the mean part retains the familiar formulation:

$$\bar{\tau}^*_{\mathrm{tot},xx} = (\bar{\mu} + \bar{\mu}_t)\left(\frac{4}{3}\frac{\partial\bar{u}}{\partial x} - \frac{2}{3}\frac{\partial\bar{v}}{\partial y}\right) \tag{27}$$

Consequently, the problem of closure in respect to the unknown Reynolds stresses is reduced to the modeling of the perturbed and mean eddy viscosities $\tilde{\mu}^*_t$ and $\bar{\mu}_t$, respectively. Furthermore, a law governing the perturbed molecular viscosity $\tilde{\mu}^*$ has to be derived. The component $\bar{\mu}$ is obtained directly from Eq. (10) when inserting the mean static temperature $\bar{T}^*$.

In this context, triple decomposition and linearization of the energy equation contained in Eq. (1) are far more complex than for the momentum equations. Undergoing the already described process, a variety of turbulent energy correlation terms, such as Reynolds stress work and turbulent heat fluxes, has to be localized in the convective fluxes and appropriately incorporated into the viscous fluxes. Taking Π_x from Eq. (7), for example, we eventually obtain

$$\tilde{\Pi}^*_x = \bar{u}\tilde{\tau}^*_{\mathrm{tot},xx} + \bar{v}\tilde{\tau}^*_{\mathrm{tot},xy} + \tilde{u}\bar{\tau}^*_{\mathrm{tot},xx} + \tilde{v}\bar{\tau}^*_{\mathrm{tot},xy} - \tilde{q}^*_{\mathrm{tot},x} \tag{28}$$

for the perturbed component, whereas the mean part yields

$$\bar{\Pi}^*_x = \bar{u}\bar{\tau}^*_{\mathrm{tot},xx} + \bar{v}\bar{\tau}^*_{\mathrm{tot},xy} - \bar{q}^*_{\mathrm{tot},x} \tag{29}$$

Again falling back on Boussinesq, turbulent heat-flux terms are accounted for in the composites $\tilde{q}^*_{\mathrm{tot},x}$ and $\bar{q}^*_{\mathrm{tot},x}$ through the perturbed and mean temperature gradients in conjunction with the decomposed eddy viscosity. Hence, the linearized perturbation of the total heat flux is governed by

$$\tilde{q}^*_{\mathrm{tot},x} = -\frac{\gamma}{\gamma-1}\left[\left(\frac{\bar{\mu}}{Pr} + \frac{\bar{\mu}_t}{Pr_t}\right)\frac{\partial\tilde{T}^*}{\partial x} + \left(\frac{\tilde{\mu}^*}{Pr} + \frac{\tilde{\mu}^*_t}{Pr_t}\right)\frac{\partial\bar{T}^*}{\partial x}\right] \tag{30}$$

with the mean counterpart formulated in familiar fashion as

$$\bar{q}^*_{\mathrm{tot},x} = -\frac{\gamma}{\gamma-1}\left(\frac{\bar{\mu}}{Pr} + \frac{\bar{\mu}_t}{Pr_t}\right)\frac{\partial\bar{T}^*}{\partial x} \tag{31}$$

Time-Domain Formulation

Consistent application of the triple decomposition to the instantaneous Navier–Stokes equations, while treating higher-order terms and turbulent correlations, results in the time-linearized governing equations of the perturbed flow.[15] Casting the equations in a strong conservation form equivalent to Eq. (1) yields

$$\frac{\partial\tilde{\boldsymbol{Q}}^*}{\partial\tau} + \frac{\partial\tilde{\boldsymbol{F}}^*}{\partial\xi} + \frac{\partial\tilde{\boldsymbol{G}}^*}{\partial\eta} = \frac{\partial\tilde{\boldsymbol{F}}^*_v}{\partial\xi} + \frac{\partial\tilde{\boldsymbol{G}}^*_v}{\partial\eta} \tag{32}$$

Time dependency is now restricted to the unknown perturbed quantities, which appear only in linear combinations with established mean quantities throughout the equation system. In this regard the transformed state vector $\tilde{\boldsymbol{Q}}^*$ decomposes into

$$\tilde{\boldsymbol{Q}}^* = \bar{J}\tilde{\boldsymbol{q}}^* + \tilde{J}^*\bar{\boldsymbol{q}}^* \tag{33}$$

the linearized Cartesian vectors of the perturbed and mean conservative variables being

$$\tilde{\boldsymbol{q}}^* = (\tilde{\rho}, \widetilde{\rho u}^*, \widetilde{\rho v}^*, \widetilde{\rho e}^*)^T, \qquad \bar{\boldsymbol{q}}^* = (\bar{\rho}, \overline{\rho u}^*, \overline{\rho v}^*, \overline{\rho e}^*)^T \tag{34}$$

With the exception of density, elements appearing in Eq. (34) are defined by use of perturbed and mean primitive variables, for example, the momentum in Cartesian x direction is given by

$$\widetilde{\rho u}^* := \bar{\rho}\tilde{u} + \tilde{\rho}\bar{u}, \qquad \overline{\rho u}^* := \bar{\rho}\bar{u} \tag{35}$$

Closing the Equation System

Pressure

Applying the presented decomposition and linearization techniques to the thermal equation of state, connectivity between the perturbed static temperature and pressure is achieved per $\tilde{T}^* = (\tilde{p}^* - \tilde{\rho}\bar{T}^*)/\bar{\rho}$ supplemented by $\bar{T}^* = \bar{p}^*/\bar{\rho}$. In analogy, formulations for $\tilde{p}^*$ and $\bar{p}^*$ as functions of the decomposed conservative variables are obtained through Eq. (9). Disregrading turbulent kinetic energy terms emerging from the averaging process, the linearized law governing $\tilde{p}^*$ becomes equivalent to the one used for closing the small disturbance Euler equations.[4] Likewise, $\bar{p}^*$ results directly from inserting the linearized mean conservative variables composing $\bar{\boldsymbol{q}}^*$ into Eq. (9).

Molecular Viscosity

As Sutherland's law defies conventional decomposition into a perturbed and mean part because of its mathematical nature, an alternative approach based on a first-order Taylor-series expansion of Eq. (10) about the mean static temperature is pursued. Consequently, the perturbed molecular viscosity is calculated from the perturbed static temperature with

$$\tilde{\mu}^* = \left.\frac{\partial\mu}{\partial T}\right|_{\bar{T}^*}\cdot\tilde{T}^* = \frac{\bar{\mu}}{\bar{T}^* + S}\left[\frac{3(\bar{T}^* + S)}{2\bar{T}^*} - 1\right]\cdot\tilde{T}^* \tag{36}$$

satisfying the small disturbance consideration.

Eddy Viscosity

In the present study the Spalart–Allmaras turbulence model[16] is employed for calculating the perturbed as well as the mean eddy viscosity throughout the flowfield. Constructed as one additional partial differential equation, its incorporation into the existing equation system is not only straightforward, but more importantly lends itself to a complete small disturbance formulation.[8] As the model's auxiliary functions are all continuosly differentiable, a Taylor-series expansion becomes feasible, when standard decomposition fails. The basic turbulence model accounts for convection, diffusion, production, and destruction of the eddy viscosity μ_t as formulated in terms of the conservative working variable $\breve{\mu} := \rho\breve{\nu}$. The relationship between μ_t and $\breve{\mu}$ is given through

$$\mu_t = \breve{\mu} f_{v1}, \qquad \text{with} \qquad f_{v1} = \chi^3 \big/ \left(\chi^3 + c_{v1}^3\right)$$
$$\text{and} \qquad \chi := \breve{\mu}/\mu \tag{37}$$

Written in strong conservation form for curvilinear coordinates, the equation governing $\breve{\mu}$ becomes formally similiar to Eq. (1) and therefore is easily included into the Navier–Stokes equation system as

$$\frac{\partial Q_5}{\partial \tau} + \frac{\partial F_5}{\partial \xi} + \frac{\partial G_5}{\partial \eta} = \frac{\partial F_{v5}}{\partial \xi} + \frac{\partial G_{v5}}{\partial \eta} + T_5 \tag{38}$$

The fifth components of the solution vector, the generalized convective, and viscous flux vectors are specified to

$$Q_5 = J\breve{\mu}, \qquad E_{5\psi} = \breve{\mu}\theta_\psi, \qquad E_{v5\psi} = J\psi_x \tau_{\breve{\mu}x} + J\psi_y \tau_{\breve{\mu}y} \tag{39}$$

The viscous flux component $E_{v5\psi}$ is constructed to allow for second-order diffusion in respect to $\breve{\mu}$, with the appearing viscous shear-stress equivalent terms defined through

$$\tau_{\breve{\mu}x} = \frac{\mu + \breve{\mu}}{\sigma} \frac{\partial}{\partial x}\left(\frac{\breve{\mu}}{\rho}\right), \qquad \tau_{\breve{\mu}y} = \frac{\mu + \breve{\mu}}{\sigma} \frac{\partial}{\partial y}\left(\frac{\breve{\mu}}{\rho}\right) \tag{40}$$

Turbulent production, destruction, and first-order diffusion are composited into the source term

$$T_5 = J(P_{\breve{\mu}} + D_{\breve{\mu}} + F_{\breve{\mu}}) \tag{41}$$

with production being governed by

$$P_{\breve{\mu}} = c_{b1}|\breve{\omega}|\breve{\mu} \qquad \text{and} \qquad |\breve{\omega}| = |\omega| + (\breve{\mu}/\rho\kappa^2 d^2) f_{v2} \tag{42}$$

In Eq. (42) d represents the distance of the considered field point to the nearest wall, and $|\omega|$ substitutes for the magnitude of vorticity, while f_{v2} provides near-wall dampening:

$$|\omega| = \left|\frac{\partial v}{\partial x} - \frac{\partial u}{\partial y}\right|, \qquad f_{v2} = 1 - \frac{\chi}{1 + \chi f_{v1}} \tag{43}$$

Furthermore, turbulent destruction is considered through

$$D_{\breve{\mu}} = -\frac{c_{w1} f_w}{\rho}\left(\frac{\breve{\mu}}{d}\right)^2 \qquad \text{and} \qquad f_w = g\left(\frac{1 + c_{w3}^6}{g^6 + c_{w3}^6}\right)^{\frac{1}{6}} \tag{44}$$

with the auxiliary expressions

$$g = r + c_{w2}(r^6 - r) \qquad \text{and} \qquad r = \breve{\mu}/\rho|\breve{\omega}|\kappa^2 d^2 \tag{45}$$

Utilizing the nabla operator $\boldsymbol{\nabla}$, first-order diffusion is expressed compactly as

$$F_{\breve{\mu}} = (\rho c_{b2}/\sigma)[\boldsymbol{\nabla}(\breve{\mu}/\rho)]^2 \tag{46}$$

The calibration constants c_{v1}, σ, c_{b1}, c_{b2}, κ, c_{w1}, c_{w2}, and c_{w3} appearing in Eqs. (37–46) are given in Ref. 16. Only fully turbulent flow is considered in this context, that is, no modeling of transition is contained in the preceding equations.

Consistent application of the discussed linearization techniques to the Spalart–Allmaras turbulence model yields a small disturbance formulation for the equations governing the perturbed eddy viscosity $\tilde{\mu}_t^*$. In analogy $\tilde{\mu}_t^*$ is dependent on the perturbed as well as the mean component of the working variable $\tilde{\breve{\mu}}^*$ and $\bar{\breve{\mu}}$, respectively. Conforming with Eq. (35), $\tilde{\breve{\mu}}^*$ itself decomposes into linear terms of its perturbed and mean primitive quantities $\tilde{\breve{\mu}}^* := \bar{\rho}\tilde{\breve{\nu}} + \tilde{\rho}\bar{\breve{\nu}}$. Accordingly, $\tilde{\mu}_t^*$ is expressed through

$$\tilde{\mu}_t^* = \bar{\breve{\mu}} \tilde{f}_{v1}^* + \tilde{\breve{\mu}}^* \bar{f}_{v1}, \qquad \text{with} \qquad \tilde{f}_{v1}^* = \frac{3\bar{\chi}^2 c_{v1}^3}{\left(\bar{\chi}^3 + c_{v1}^3\right)^2}\tilde{\chi}^*$$
$$\text{and} \qquad \tilde{\chi}^* := \bar{\mu}^{-2}\left(\bar{\mu}\tilde{\breve{\mu}}^* - \tilde{\mu}^*\bar{\breve{\mu}}\right) \tag{47}$$

As becomes evident in Eq. (47), mean values of functions or supplemental quantities associated with the Spalart–Allmaras turbulence model will appear throughout the following time-linearized equations. Denoted by –, they are obtained directly when expressing Eqs. (37–46) for the steady state, that is, the formulation required when calculating $\bar{\mu}_t$.

The strong conservation form of Eq. (38) is retained by the equation governing $\tilde{\breve{\mu}}^*$

$$\frac{\partial \tilde{Q}_5^*}{\partial \tau} + \frac{\partial \tilde{F}_5^*}{\partial \xi} + \frac{\partial \tilde{G}_5^*}{\partial \eta} = \frac{\partial \tilde{F}_{v5}^*}{\partial \xi} + \frac{\partial \tilde{G}_{v5}^*}{\partial \eta} + \tilde{T}_5^* \tag{48}$$

allowing its incorporation into the time-linearized perturbed flow equation system Eq. (32). The fifth components of the perturbed solution vector and generalized convective flux are derived as

$$\tilde{Q}_5^* = \bar{J}\tilde{\breve{\mu}}^* + \tilde{J}^*\bar{\breve{\mu}}, \qquad \tilde{E}_{5\psi}^* = \bar{\breve{\mu}}\tilde{\theta}_\psi^{(1)} + \bar{\breve{\mu}}\tilde{\theta}_\psi^{(2)} + \tilde{\breve{\mu}}^*\bar{\theta}_\psi \tag{49}$$

respectively. Through the decomposition three forms of the modified generalized contravariant velocity arise in $\tilde{E}_{5\psi}^*$:

$$\tilde{\theta}_\psi^{(1)} = \overline{J\psi}_x \tilde{u} + \overline{J\psi}_y \tilde{v}, \qquad \tilde{\theta}_\psi^{(2)} = \widetilde{J\psi}^*_x \bar{u} + \widetilde{J\psi}^*_y \bar{v} + \widetilde{J\psi}^*_t$$
$$\bar{\theta}_\psi = \overline{J\psi}_x \bar{u} + \overline{J\psi}_y \bar{v} \tag{50}$$

On one hand $\tilde{\theta}_\psi^{(1)}$ contains only combinations of the perturbed velocities with the mean metrics, whereas on the other hand $\tilde{\theta}_\psi^{(2)}$ is composited by mean velocities and the perturbed metrics, that is, complementary to $\tilde{\theta}_\psi^{(1)}$. $\bar{\theta}_\psi$ being the mean state of Eq. (5). Likewise, the fifth component of the generalized viscous flux separates into

$$\tilde{E}_{v5\psi}^* = \overline{J\psi}_x \tilde{\tau}_{\breve{\mu}x}^* + \overline{J\psi}_y \tilde{\tau}_{\breve{\mu}y}^* + \widetilde{J\psi}^*_x \bar{\tau}_{\breve{\mu}x} + \widetilde{J\psi}^*_y \bar{\tau}_{\breve{\mu}y} \tag{51}$$

with $\tilde{\tau}_{\breve{\mu}x}^*$ and $\tilde{\tau}_{\breve{\mu}y}^*$ representing the perturbed parts of the viscous shear-stress equivalent terms, for example,

$$\tilde{\tau}_{\breve{\mu}x}^* = \frac{\bar{\mu} + \bar{\breve{\mu}}}{\sigma}\frac{\partial}{\partial x}\left(\frac{\tilde{\breve{\mu}}^*}{\bar{\rho}} - \bar{\breve{\mu}}\frac{\tilde{\rho}^*}{\bar{\rho}^2}\right) + \frac{\tilde{\mu} + \tilde{\breve{\mu}}^*}{\bar{\mu} + \bar{\breve{\mu}}}\bar{\tau}_{\breve{\mu}x} \tag{52}$$

$\tilde{\tau}_{\breve{\mu}y}^*$ is obtained directly by substituting the partial derivative $\partial/\partial x$ in Eq. (52) with $\partial/\partial y$ and $\bar{\tau}_{\breve{\mu}x}$ with $\bar{\tau}_{\breve{\mu}y}$. Continuing in a similar manner, the perturbation of the turbulent source term is expressed through

$$\tilde{T}_5^* = \bar{J}\left(\tilde{P}_{\breve{\mu}}^* + \tilde{D}_{\breve{\mu}}^* + \tilde{F}_{\breve{\mu}}^*\right) + \tilde{J}^*(\bar{P}_{\breve{\mu}} + \bar{D}_{\breve{\mu}} + \bar{F}_{\breve{\mu}}) \tag{53}$$

with production being governed by the following set of equations:

$$\tilde{P}_{\breve{\mu}}^* = \bar{P}_{\breve{\mu}} \cdot \left(\frac{\tilde{\breve{\mu}}^*}{\bar{\breve{\mu}}} + \frac{|\tilde{\breve{\omega}}|^*}{|\bar{\breve{\omega}}|}\right), \quad \Delta|\bar{\omega}| = |\bar{\breve{\omega}}| - |\bar{\omega}| \tag{54}$$

$$|\tilde{\breve{\omega}}|^* = |\tilde{\omega}|^* + \Delta|\bar{\omega}|\left(\frac{\tilde{f}_{v2}^*}{\bar{f}_{v2}} + \frac{\tilde{\breve{\mu}}^*}{\bar{\breve{\mu}}} - \frac{\tilde{\rho}}{\bar{\rho}} - 2\frac{\tilde{d}}{\bar{d}}\right) \tag{55}$$

Equation (55) utilizes linearized formulations of the magnitude of vorticity and the near-wall dampening function, derived as

$$|\tilde{\omega}|^* = |\bar{\omega}|^{-1}\left(\frac{\partial \bar{v}}{\partial x} - \frac{\partial \bar{u}}{\partial y}\right)\left(\frac{\partial \tilde{v}}{\partial x} - \frac{\partial \tilde{u}}{\partial y}\right)$$
$$\text{and} \qquad \tilde{f}_{v2}^* = \frac{\tilde{f}_{v1}^* \bar{\chi}^2 - \tilde{\chi}^*}{(1 + \bar{f}_{v1}\bar{\chi})^2} \tag{56}$$

respectively. Furthermore, perturbed turbulent destruction obeys

$$\tilde{D}^*_{\breve{\mu}} = \bar{D}_{\breve{\mu}} \cdot \left(\frac{\tilde{f}^*_w}{\bar{f}_w} + 2\frac{\breve{\tilde{\mu}}^*}{\breve{\bar{\mu}}} - \frac{\tilde{\rho}}{\bar{\rho}} - 2\frac{\tilde{d}}{\bar{d}} \right)$$

$$\text{and} \qquad \tilde{f}^*_w = \frac{\bar{f}_w}{\bar{g}} \left(\frac{c^6_{w3}}{\bar{g}^6 + c^6_{w3}} \right) \tilde{g}^* \tag{57}$$

with the auxiliary expressions

$$\tilde{g}^* = \left[1 + c_{w2}(6\bar{r}^5 - 1) \right] \tilde{r}^*$$

$$\text{and} \qquad \tilde{r}^* = \bar{r} \left(\frac{\breve{\tilde{\mu}}^*}{\breve{\bar{\mu}}} - \frac{\tilde{\rho}}{\bar{\rho}} - \frac{|\breve{\tilde{\omega}}|^*}{|\breve{\bar{\omega}}|} - 2\frac{\tilde{d}}{\bar{d}} \right) \tag{58}$$

Finally, the linearized formulation of the first-order diffusion term yields

$$\tilde{F}^*_{\breve{\mu}} = \frac{2\bar{\rho} c_{b2}}{\sigma} \nabla \left(\frac{\breve{\bar{\mu}}}{\bar{\rho}} \right) \left[\nabla \left(\frac{\breve{\tilde{\mu}}^*}{\bar{\rho}} \right) - \nabla \left(\frac{\breve{\bar{\mu}} \tilde{\rho}}{\bar{\rho}^2} \right) \right] + \frac{\tilde{\rho}}{\bar{\rho}} \bar{F}_{\breve{\mu}} \tag{59}$$

Small-Disturbance Navier–Stokes Equations

Having provided closure and subsequently incorporating the turbulence model into Eq. (32), the time-linearized perturbed flow equation is subject to slight rearrangement in preparation of a frequency-domain formulation.

As has become evident, for example, in Eq. (50), decomposition and time-linearization yielded two basic sets of terms throughout the equation system: The first group, to be denoted by superscript (1), exclusively contains the unknown perturbed flow quantities appearing in linear combination with mean flow quantities or metrics, that is, they are homogenous in the perturbed solution vector $\tilde{\boldsymbol{q}}^*$. The complementary second group, hence distinguished by superscript (2), solely consists of the perturbed metrics in linear combination with the mean flow quantities. All terms collected in group (2) are designated as known because of the following considerations: The deformation of the computational grid is prescribed through the body's periodic motion, consequently supplying the perturbed metrics. Similar, the mean flow quantities can be provided in advance by a steady-state RANS solution for the body's mean, that is, reference, position. Hence, reformulation of the time-linearized perturbed flow equations as detailed in Ref. 17 isolates the (2) denoted vector components on the right-hand side of the equation system:

$$\frac{\partial \tilde{\boldsymbol{Q}}^{(1)}}{\partial \tau} + \frac{\partial \left[\tilde{\boldsymbol{F}}^{(1)} - \tilde{\boldsymbol{F}}^{(1)}_v \right]}{\partial \xi} + \frac{\partial \left[\tilde{\boldsymbol{G}}^{(1)} - \tilde{\boldsymbol{G}}^{(1)}_v \right]}{\partial \eta}$$

$$= -\left[\frac{\partial \tilde{\boldsymbol{Q}}^{(2)}}{\partial \tau} + \frac{\partial \left[\tilde{\boldsymbol{F}}^{(2)} - \tilde{\boldsymbol{F}}^{(2)}_v \right]}{\partial \xi} + \frac{\partial \left[\tilde{\boldsymbol{G}}^{(2)} - \tilde{\boldsymbol{G}}^{(2)}_v \right]}{\partial \eta} \right]$$

$$+ \tilde{\boldsymbol{T}}^{(1)} + \tilde{\boldsymbol{T}}^{(2)} \tag{60}$$

It is obvious from Eq. (60) that the (2) components are exclusively responsible for initiating the development of the perturbed solution and therefore are considered as the equation system's source terms.

Restriction of the body's motion to a harmonic oscillation allows the perturbed coordinates of the grid deformation to be expressed as

$$\tilde{x}(\xi, \eta, \tau) = \hat{x}(\xi, \eta) \cdot e^{ik\tau}, \qquad \tilde{y}(\xi, \eta, \tau) = \hat{y}(\xi, \eta) \cdot e^{ik\tau} \tag{61}$$

having been decomposed into a time-invariant amplitude and the respective complex time law $e^{ik\tau}$. As the motion is prescribed, the angular frequency k is known. Consequently, the linearized perturbed cell volume and metrics result in

$$\tilde{J}^* := \hat{J}^* \cdot e^{ik\tau}, \qquad \widetilde{J\psi}^*_{x,y,t} := \widehat{J\psi}^*_{x,y,t} \cdot e^{ik\tau} \tag{62}$$

respectively. To avoid double notation, from this point on superscript $*$ will be dropped in connection with superscript $\hat{}$ as the indicator of linearity. Modeling of the flow response occurs in similar manner: The perturbation of an arbitrary field quantity is defined as

$$\tilde{\Phi}(\xi, \eta, \tau) := \hat{\Phi}(\xi, \eta) \cdot e^{ik\tau} \tag{63}$$

with $\hat{\Phi}$ representing the quantity's complex amplitude. Expressing each individual primitive perturbation variable appearing in Eq. (60) according to Eq. (63) results in a corresponding separation for the homogenous vector components:

$$\tilde{\boldsymbol{Q}}^{(1)} = \hat{\boldsymbol{Q}}^{(1)} \cdot e^{ik\tau}, \qquad \tilde{\boldsymbol{E}}^{(1)}_{\psi} = \hat{\boldsymbol{E}}^{(1)}_{\psi} \cdot e^{ik\tau}, \qquad \tilde{\boldsymbol{E}}^{(1)}_{v\psi} = \hat{\boldsymbol{E}}^{(1)}_{v\psi} \cdot e^{ik\tau}$$

$$\tilde{\boldsymbol{T}}^{(1)} = \hat{\boldsymbol{T}}^{(1)} \cdot e^{ik\tau} \tag{64}$$

Likewise, $\tilde{J}^*$ and $\widetilde{J\psi}^*_{x,y,t}$ contained in the (2) vector components of Eq. (60) are replaced with Eq. (62). As the time law $e^{ik\tau}$ now appears linearily in all components of the equation system, it can be eliminated completely. Thus, a formulation for the time-invariant amplitude quantities of the flow perturbation is obtained. Recasting the governing equations for the complex amplitude of the state vector, that is,

$$\hat{\boldsymbol{Q}}^{(1)} = \bar{J}\hat{\boldsymbol{q}} = \bar{J}(\hat{\rho}, \widehat{\rho u}, \widehat{\rho v}, \widehat{\rho e}, \hat{\breve{\mu}})^T \tag{65}$$

ultimately yields the small disturbance Navier–Stokes equations:

$$\frac{\partial \hat{\boldsymbol{Q}}^{(1)}}{\partial \tau} + \frac{\partial \left[\hat{\boldsymbol{F}}^{(1)} - \hat{\boldsymbol{F}}^{(1)}_v \right]}{\partial \xi} + \frac{\partial \left[\hat{\boldsymbol{G}}^{(1)} - \hat{\boldsymbol{G}}^{(1)}_v \right]}{\partial \eta} = \hat{\boldsymbol{S}}^{(1)} + \hat{\boldsymbol{S}}^{(2)} \tag{66}$$

The newly introduced source components $\hat{\boldsymbol{S}}^{(1)}$ and $\hat{\boldsymbol{S}}^{(2)}$ substitute for

$$\hat{\boldsymbol{S}}^{(1)} = -ik\hat{\boldsymbol{Q}}^{(1)} + \hat{\boldsymbol{T}}^{(1)} \tag{67}$$

$$\hat{\boldsymbol{S}}^{(2)} = -\left\{ ik\hat{\boldsymbol{Q}}^{(2)} + \frac{\partial \left[\hat{\boldsymbol{F}}^{(2)} - \hat{\boldsymbol{F}}^{(2)}_v \right]}{\partial \xi} + \frac{\partial \left[\hat{\boldsymbol{G}}^{(2)} - \hat{\boldsymbol{G}}^{(2)}_v \right]}{\partial \eta} \right\} + \hat{\boldsymbol{T}}^{(2)} \tag{68}$$

Furthermore, the homogenous convective flux vectors are obtained directly through the generalized mean Jacobian matrix multiplied by the Cartesian amplitude state vector:

$$\hat{\boldsymbol{E}}^{(1)}_{\psi} = \left. \frac{\partial \boldsymbol{E}_{\psi}}{\partial \boldsymbol{q}} \right|_{\bar{q}} \cdot \hat{\boldsymbol{q}} = \bar{\boldsymbol{K}}_{\psi} \cdot \hat{\boldsymbol{q}} \tag{69}$$

$$\bar{\boldsymbol{K}}_{\psi} = \begin{pmatrix} 0 & \overline{J\psi}_x & \overline{J\psi}_y & 0 & 0 \\ \overline{J\psi}_x\bar{\phi} - \bar{u}\bar{\theta}_{\psi} & \bar{\theta}_{\psi} + (2-\gamma)\overline{J\psi}_x\bar{u} & \overline{J\psi}_y\bar{u} - (\gamma-1)\overline{J\psi}_x\bar{v} & (\gamma-1)\overline{J\psi}_x & 0 \\ \overline{J\psi}_y\bar{\phi} - \bar{v}\bar{\theta}_{\psi} & \overline{J\psi}_x\bar{v} - (\gamma-1)\overline{J\psi}_y\bar{u} & \bar{\theta}_{\psi} + (2-\gamma)\overline{J\psi}_y\bar{v} & (\gamma-1)\overline{J\psi}_y & 0 \\ (2\bar{\phi} - \gamma\bar{e})\bar{\theta}_{\psi} & (\gamma\bar{e} - \bar{\phi})\overline{J\psi}_x - (\gamma-1)\bar{\theta}_{\psi}\bar{u} & (\gamma\bar{e} - \bar{\phi})\overline{J\psi}_y - (\gamma-1)\bar{\theta}_{\psi}\bar{v} & \gamma\bar{\theta}_{\psi} & 0 \\ -\breve{\bar{\mu}}/\bar{\rho}\bar{\theta}_{\psi} & \breve{\bar{\mu}}/\bar{\rho}\overline{J\psi}_x & \breve{\bar{\mu}}/\bar{\rho}\overline{J\psi}_y & 0 & \bar{\theta}_{\psi} \end{pmatrix}$$

$$\text{with} \qquad \bar{\theta}_{\psi} = \overline{J\psi}_x\bar{u} + \overline{J\psi}_y\bar{v}, \qquad \bar{\phi} = [(\gamma-1)/2](\bar{u}^2 + \bar{v}^2) \tag{70}$$

The homogenous viscous flux and the turbulent source-term vector result in

$$\hat{\boldsymbol{E}}^{(1)}_{v\psi} = \begin{pmatrix} 0 \\ \overline{J\psi}_x \hat{\tau}_{xx} + \overline{J\psi}_y \hat{\tau}_{yx} \\ \overline{J\psi}_x \hat{\tau}_{xy} + \overline{J\psi}_y \hat{\tau}_{yy} \\ \overline{J\psi}_x \hat{\Pi}_x + \overline{J\psi}_y \hat{\Pi}_y \\ \overline{J\psi}_x \hat{\tau}_{\breve{\mu}x} + \overline{J\psi}_y \hat{\tau}_{\breve{\mu}y} \end{pmatrix} \tag{70}$$

$$\hat{\boldsymbol{T}}^{(1)} = \bar{J} \begin{pmatrix} 0 \\ 0 \\ 0 \\ 0 \\ \hat{P}_{\breve{\mu}} + \hat{D}_{\breve{\mu}} + \hat{F}_{\breve{\mu}} \end{pmatrix} \tag{71}$$

respectively. Amplitude terms contained in Eqs. (71) and (72), for example, $\hat{\tau}_{xx}$, $\hat{\Pi}_x$, $\hat{\tau}_{\breve{\mu}x}$, or $\hat{P}_{\breve{\mu}}$, are expressed through the respective perturbed formulations derived earlier by replacing the ˜ modifier with ˆ. For the sake of clarity, the index tot has been dropped from the viscous shear-stress and energy flux terms. Finally, the vector components compositing $\hat{\boldsymbol{S}}^{(2)}$ yield

$$\hat{\boldsymbol{Q}}^{(2)} = \hat{J}\bar{\boldsymbol{q}} = \hat{J}\left(\bar{\rho}, \overline{\rho u}, \overline{\rho v}, \overline{\rho e}, \breve{\bar{\mu}}\right)^T \tag{72}$$

$$\hat{\boldsymbol{E}}^{(2)}_{\psi} = \begin{pmatrix} \bar{\rho}\hat{\theta}^{(2)}_{\psi} \\ \overline{\rho u}\hat{\theta}^{(2)}_{\psi} + \widehat{J\psi}_x \bar{p} \\ \overline{\rho v}\hat{\theta}^{(2)}_{\psi} + \widehat{J\psi}_y \bar{p} \\ \bar{H}\hat{\theta}^{(2)}_{\psi} - \widehat{J\psi}_t \bar{p} \\ \breve{\bar{\mu}}\hat{\theta}^{(2)}_{\psi} \end{pmatrix} \tag{73}$$

$$\hat{\boldsymbol{E}}^{(2)}_{v\psi} = \begin{pmatrix} 0 \\ \widehat{J\psi}_x \bar{\tau}_{xx} + \widehat{J\psi}_y \bar{\tau}_{yx} \\ \widehat{J\psi}_x \bar{\tau}_{xy} + \widehat{J\psi}_y \bar{\tau}_{yy} \\ \widehat{J\psi}_x \bar{\Pi}_x + \widehat{J\psi}_y \bar{\Pi}_y \\ \widehat{J\psi}_x \bar{\tau}_{\breve{\mu}x} + \widehat{J\psi}_y \bar{\tau}_{\breve{\mu}y} \end{pmatrix} \tag{74}$$

$$\hat{\boldsymbol{T}}^{(2)} = \hat{J} \begin{pmatrix} 0 \\ 0 \\ 0 \\ 0 \\ \bar{P}_{\breve{\mu}} + \bar{D}_{\breve{\mu}} + \bar{F}_{\breve{\mu}} \end{pmatrix} \tag{75}$$

and

$$\hat{\theta}^{(2)}_{\psi} = \widehat{J\psi}_x \bar{u} + \widehat{J\psi}_y \bar{v} + \widehat{J\psi}_t \tag{76}$$

With the derivation of the small disturbance Navier–Stokes equations, the initial unsteady problem has been reduced to a steady one for the complex amplitude flow quantities. As $\hat{\boldsymbol{Q}}^{(1)}$ is invariant to time, the derivative $\partial\hat{\boldsymbol{Q}}^{(1)}/\partial\tau$ consequently would vanish from Eq. (66). However, it is retained in the formulation in order to construct a pseudo-time-marching solution scheme, thus artifically preserving the equation system's time hyberbolic mathematical nature. Coupling between the in-phase (real) and out-of-phase (imaginary) parts of the complex equation system is solely provided by $ik\hat{\boldsymbol{Q}}^{(1)}$. For $k = 0$, that is, the quasi-steady case, this interaction is eliminated, therefore restricting the solution to the real part. Letting $Re_\infty \to \infty$, while disregarding the turbulence model incorporated into Eq. (66), yields the small disturbance Euler equations as given in Ref. 4. Thus, implementing the small disturbance Navier–Stokes method FLM-SD.NS on basis of the existing small disturbance Euler solver FLM-SDEu becomes reasonable. The definitions for the linearized amplitude volume $\hat{J}$ and metrics $\widehat{J\psi}_{x,y,t}$ appearing throughout Eqs. (73–77) are also taken from Ref. 4.

Numerical Method

General Properties

The numerical algorithm for solving Eq. (66) is constructed by incorporating the derived viscous and turbulence modeling components into the FLM-SDEu code. In this way the total-variation-diminishing property, Roe's convective flux-difference splitting and the second-order spatial accuracy of the existing inviscid finite volume approach[4] are fully retained. Furthermore, with the introduction of the viscous fluxes and turbulence source term, Cartesian gradients of the primitive mean and amplitude quantities now have to be treated as well. For evaluation of these first derivatives, Chakravarthy's application of Gauss's integral theorem in high-resolution schemes is employed.[18] The mean gradients are calculated through the basic method, whereas the assessment of the amplitude gradients occurs with a corresponding small disturbance formulation as detailed in Ref. 19. Replacing the original explicit Runge–Kutta pseudo-time-stepping scheme with an implict lower-upper symmetric successive overrelaxation (LU-SSOR) approach embedded in a multigrid algorithm enhances the performance of the solution process. Originating from the work of Jameson and Turkel,[20] efficient coupling of the LU-SSOR scheme with a multigrid technique has been realized and thoroughly investigated by Blazek[21,22] for the steady-state RANS equations. Retaining the properities of LU-SSOR, which is characterized by a diagonally dominant factorization, a corresponding small disturbance formulation for solving Eq. (66) has been derived and implemented.[23] Consistent treatment of the adiabatic wall and no-slip boundary conditions and their discrete formulation[19] completes the extension of FLM-SDEu to FLM-SD.NS. In developing FLM-SD.NS, special care has been taken to maintain numerical equivalency with the second-order time-accurate RANS solver FLM-NS,[24] which has recently been updated with the Spalart–Allmaras turbulence model[16] and the multigrid technique.[21,22] As FLM-NS features the original nonlinearized formulations of the discretization and integration schemes implemented in FLM-SD.NS, comparability between the time-accurate, that is, dynamically fully nonlinear, and the small disturbance method exists.

Simulation Process

In a first step two computational grids are supplied: one for the reference position of the body and the other for the deflected extremum position, generated through deformation. A turbulent steady-state solution then is produced with FLM-NS in the reference grid. It serves as input to FLM-SD.NS, providing the prerequisite mean flow values as contained in the source term $\hat{\boldsymbol{S}}^{(2)}$ and the convective flux Jacobian $\bar{\boldsymbol{K}}_\psi$, Eqs. (68) and (70), respectively. Furthermore, subtraction of the reference grid from the extremum grid by FLM-SD.NS during procedure initialization yields the amplitudes of the vertices' coordinates, consequently supplying the required amplitude volume $\hat{J}$ and metrics $\widehat{J\psi}_{x,y,t}$. The components $\hat{\boldsymbol{S}}^{(2)}$ and $\bar{\boldsymbol{K}}_\psi$ are calculated only once at the beginning of the procedure and kept in storage, as they remain invariant throughout the psuedo-time-integration process. With FLM-SD.NS the first harmonic of the unsteady flow solution is obtained directly in form of the amplitude state vector's real and imaginary part.

In contrast FLM-NS only uses the steady-state solution for initialization of the time-accurate unsteady computation, which is performed through conventional dual time stepping. The required mesh movement is realized by interpolating intermediary grids between the extremum and reference position according to the time law, that is, Eq. (11) with Eq. (61). Consequently, the complete unsteady solution evolves in the time domain, requiring a Fourier analysis in postprocessing for the extraction of the desired first harmonics.

Validation Results

The validity of FLM-SD.NS (single-grid code version) in regard to subsonic laminar flow has already been successfully shown for a harmonically pitching NACA0012 airfoil,[17] with further investigations having been performed for the transonic flow regime in Ref. 25. Because of the lack of turbulence modeling and the consequential restriction to low-Reynolds-number flow, no unsteady shock boundary-layer interaction could be observed in the past simulations. With the implementation of the turbulent small disturbance Navier–Stokes code, the computation of such phenomena has now become feasible. In this context the NACA 64A010 CT8[26] and NLR 7301 CT5[27] standard test cases from AGARD-R-702 are selected for FLM-SD.NS (multigrid code version) validation at flight realistic Reynolds numbers. The harmonic motion imposed on the respective airfoil is governed by

$$\alpha(\tau) = \bar{\alpha} + \hat{\alpha} \cdot \sin(k \cdot \tau) \tag{77}$$

with case-dependent pitch axis, frequency, mean, and amplitude incidence angle. In both cases the occurence of an unsteady shock characterizes the flowfield, yet being of varying strength and thus consequence to flow separation. Calculations are performed on a Linux operating single-processor Intel® Pentium IV personal computer clocked at 2.66 GHz.

NACA 64A010 Pitch Oscillations—Weak Shock Case

The NACA 64A010 is a symmetrical airfoil of conventional type having a relative thickness of 10%. A pitch oscillation about an axis located at 25% chord length is simulated according to the just-mentioned transonic experimental test case CT8. A summary of the simulation parameters is given here, with the reduced frequency corresponding to a dimensional frequency of approximately 17 Hz: Ma_∞, 0.8; Re_∞, 12.5×10^6; $\bar{\alpha}$, 0.0 deg; $\hat{\alpha}$, 0.5 deg; k_{red}, 0.2; $\breve{T}_\infty$, 288.15 K; c_r, 1.0; and l_{Re_∞}, 1.0.

Discretization of the computational domain takes place with an elliptically smoothed structured mesh in C-topology consisting of 384 cells in circumferential and 96 cells in contour normal direction. The airfoil contour is digitized with 128 cells per side. An off-body distance of $1 \cdot 10^{-5} c_r$ for the first grid line ensures a $y^+ < 6$ as required by the Spalart–Allmaras turbulence model for viscous sublayer resolution. Additionally, cell density is increased in proximity to the airfoil contour, where shock appearance is anticipated. Both reference and deformed extremum grid are equivalent in their properties. Applying FLM-SD.NS to the unsteady flow problem, a four-level V-symmetric multigrid cycle is selected for the solution process. Per multigrid cycle dual pseudotime steps on the finest and coarsest grid levels in combination with a single pseudo time step on each of the two intermediary levels are conducted. The frequency-domain calculation is terminated after both the L_2-norm density and Spalart–Allmaras working variable residuals, as normalized with their respective values after the first multigrid cycle, have dropped below $1 \cdot 10^{-5}$. For the comparative time-accurate simulation of the CT8 test case with FLM-NS, three oscillations are computed in order to eliminate transient phenomena, each discretized with 100 physical time intervals. Multigrid settings and abort criteria are equivalent to the FLM-SD.NS solution procedure.

Assessing the prediction quality of FLM-SD.NS, an investigation of the local unsteady load distributions, that is, pressure and skin friction, on the airfoil's contour is conducted. Because the experimental data provided in AGARD-R-702[26] are limited to zeroth and first harmonic pressure coefficients c_p^0 and c_p^1, respectively, skin-friction values (c_f^0, c_f^1) are supplemented through FLOWer calculations.[28] The algebraic turbulence model according to Baldwin–Lomax[29] is employed. Developed at DLR, FLOWer is a validated time-accurate RANS solver in widespread German use. The computational mesh used in conjunction with the FLOWer calculation retains the already mentioned characteristics of the FLM-SD.NS/FLM-NS reference grid except for the off-body distance, which is reduced to $5 \cdot 10^{-6} c_r$. In this manner an equivalent evaluation of the skin friction between the vertex-centered FLOWer and the cell-centered FLM methods is realized because for both cases a wall nearest solution vector is stored at equal distance to the boundary. In contrast to the deforming mesh approach employed in FLM-NS, only a single grid for the airfoil's reference position must be supplied to FLOWer, as the method emulates the rigid-body motion by solving the RANS equations in a rotating coordinate system. Numerically, this transfers the oscillation into the far-field and no-slip wall boundary condition relative to the resting airfoil contour. The explicit dual-time-stepping scheme implemented in FLOWer and employed here is of second-order accuracy in time as well as in space. Results of FLM-SD.NS in comparison to FLM-NS, FLOWer solutions, and experimental data are composited in Fig. 1. An inviscid small disturbance solution obtained with FLM-SDEu[4] is supplied in order to evaluate the extent of viscous effects.

The pressure and skin-friction distribution's evolution over the pitch oscillation as computed with the time-accurate methods FLM-NS and FLOWer is subjected to Fourier analysis, yielding the zeroth harmonics c_p^0 and c_f^0. Comparison with the respective FLM.SD-NS counterparts reveals only minimal deviations, serving as an indication that the first and higher harmonics of the unsteady flow response have little influence on the zeroth harmonic. Therefore, the mean flow shows good conformity with the steady-state solution, which acted as input for the small disturbance method. Consequently, if the negligibility of higher harmonics holds, a flow decomposition into a mean and linear perturbation part is valid. Differences between the inviscid steady-state solution used as input for FLM-SDEu and the viscous solutions are evident for the shock region occuring at mid-chord. Initiation of the weak shock is located farther downstream with a stronger gradient and an overextended recompression before merging into the pressure recovery curve toward the trailing edge as predicted by the viscous methods. The behavior of the inviscid solution in the shock region is typical, as the boundary-layer's influence on shock formation is absent. Real and imaginary parts of the first harmonic pressure c_p^1 and skin-friction distributions c_f^1 computed with FLM-SD.NS in general exhibit good agreement with their Fourier-analyzed FLM-NS, and FLOWer equivalents. Clearly, the forward region of the airfoil is influenced mainly by the inviscid flow, the first harmonic pressure distributions predicted by the viscous methods conforming very well with the inviscid one and the experiment. Differences between FLM-SD.NS, FLM-NS, and FLOWer become evident at the shock location, the small disturbance method predicting a higher peak value than the two time-accurate methods. However, it is difficult to assess the quality of local solution accuracy in vicinty of the shock, as only one experimental data point lies within its extent. The postshock behavior of c_p^1 predicted by FLM-SD.NS again conforms excellently with both time-accurate methods and the experimental data.

Characteristically, the real part is minute, thus having little impact on the unsteadiness of the pressure distribution toward the trailing edge. In contrast the imaginary part shows greater influence, locally becoming antimetric in respect to the shock position. As to be expected, the c_p^1 distribution calculated with FLM-SDEu retains the shock characteristic peak farther downstream than the other data, as the inviscid steady-state solution served as its input. The significantly stronger and narrower peak at the shock location as well as a higher degree of unsteadiness shortly after the shock are also prominent. Again the missing influence of shock/boundary-layer interaction is evident. The viscous steady-state solution provided by FLM-NS as input to FLM-SD.NS exhibits no sign of flow reversal in the boundary layer because of the weak shock and mild adverse pressure gradient toward the trailing edge. This is put into evidence through the zeroth harmonic skin-friction distribution for FLM-SD.NS, where negative values would indicate flow reversal. The zeroth harmonic skin-friction distributions of the time-accurate methods FLM-NS and FLOWer exhibit the same behavior, thus conforming very well. Contributions to the unsteady skin-friction distribution by Rec_f^1 and Imc_f^1 are observed to a great extent in the shock/postshock regions and to a moderate degree toward the leading edge. Considering c_f^1 in conjunction with c_f^0, it becomes apparent that no unsteady flow separation is predicted throughout the oscillation.

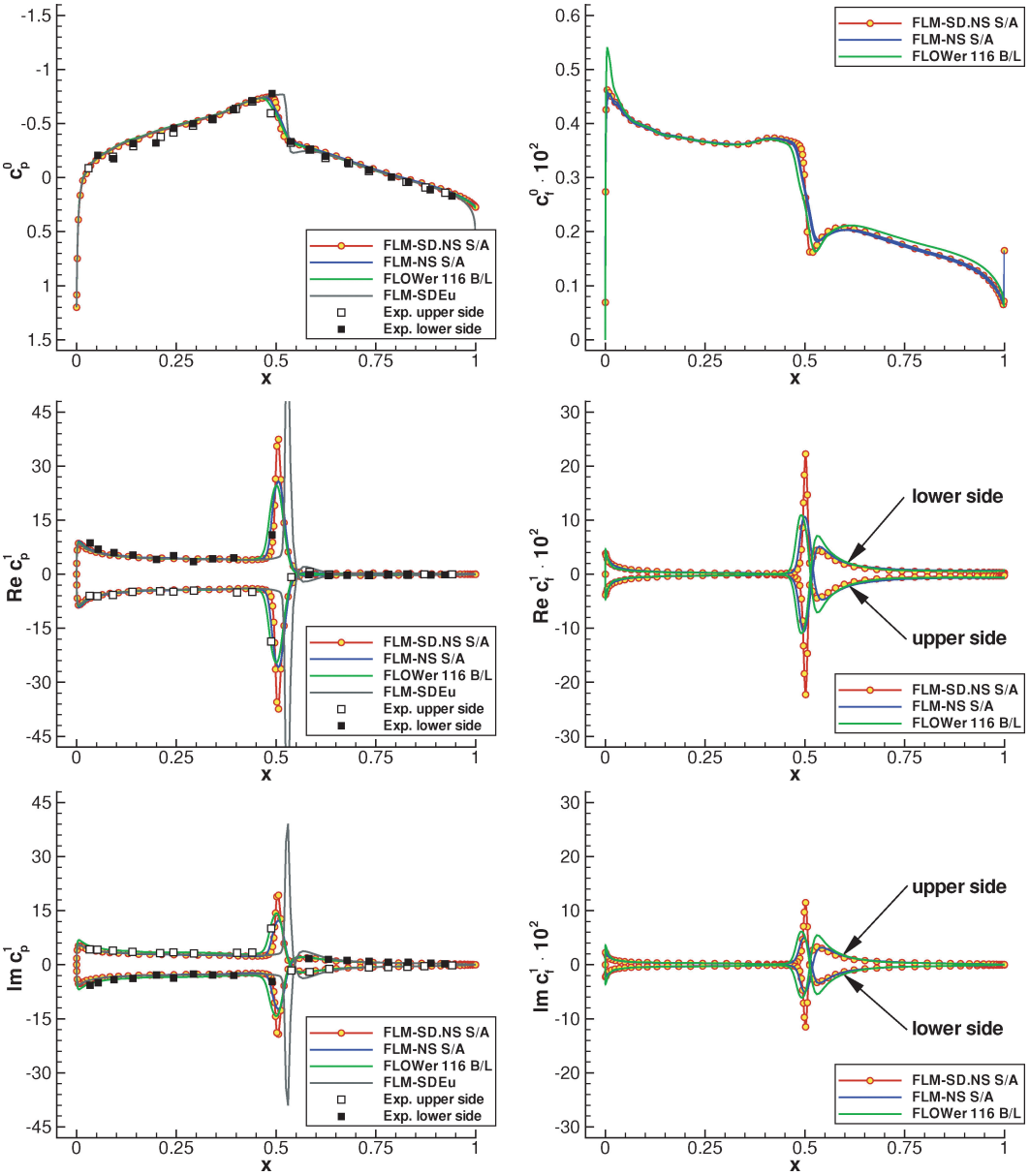

Fig. 1 Comparison of the pressure coefficient (c_p^0, c_p^1) and skin-friction coefficient (c_f^0, c_f^1) distributions for NACA 64A010 CT8 ($Ma_\infty = 0.8$, $Re_\infty = 12.5 \cdot 10^6$, $\bar{\alpha} = 0.0$ deg, $\hat{\alpha} = 0.5$ deg, $k_{\text{red}} = 0.2$).

For FLM-SD.NS in- and out-of-phase components of the lift (Rec_l^1, Imc_l^1) and pitching-moment (Rec_m^1, Imc_m^1) coefficients result directly from the integration of the respective pressure and skin-friction distributions over the airfoil contour at reference position. Having obtained a converged pseudo-steady-state solution, the process is conducted only once toward the end of the FLM-SD.NS execution. In case of the time-accurate methods FLM-NS and FLOWer, however, an integration of the pressure and skin-friction distributions must be performed after each converged physical time step of the oscillation throughout the unsteady computation. This eventually yields the c_l and c_m evolution over the angle of incidence for all cycles, including the transient ones. As periodicity of the flow is achieved in the third cycle, it is selected for comparative purposes and subjected to Fourier analysis in order to extract the coefficients' first harmonics from their respective time-dependent evolutions. The reference axis for the pitching moment coincides with the rotational axis of the pitch oscillation located at $25\%c_r$, with a positive moment defined as being tail-heavy. In this regard Table 1 summarizes the c_l^1 and c_m^1 values obtained with FLM-SD.NS, FLM-NS, and FLOWer. Agreement between the small disturbance and time-accurate methods for Rec_l^1 is excellent, the observed deviations being marginal. Excellent comformity is also given between FLM-SD.NS and FLM-NS for Imc_l^1, with FLOWer predicting a significantly higher absolute value to the contrary. Real and imaginary part of the moment coefficient c_m^1 as computed with FLM-SD.NS range from 19 to 15% higher in absolute value respective their FLM-NS counterparts, whereas only marginal deviations to the FLOWer values are apparent. The differences encountered between the two methods FLM-SD.NS and FLOWer in respect to c_m^1 already reveal the difficulty of accurately predicting the moment coefficient. Deviations of the first harmonic pressure distributions in the shock region between FLM-SD.NS and FLM-NS appear to weigh more heavily on the c_m^1 evaluation than on c_l^1, as the choice of the moment reference axis at $25\%\, c_r$ allows for a more significant contribution through leverage. Also the method specific coefficient evaluation as already detaileded has to be taken into account when assessing these values. Even though the integration procedures of FLM-NS and FLOWer are similar, a major difference exists: at each physical time step FLM-NS integrates in respect to the deflected airfoil contour within a fixed coordinate system, while FLOWer integrates in respect to the resting airfoil contour at reference position within a moving coordinate system. As the two time-accurate methods have

Table 1 NACA 64A010 CT8: Comparison of the computed global coefficients

Coefficient	FLM-SD.NS	FLM-NS	FLOWer
Rec_l^1	6.630	6.619	6.660
Imc_l^1	−3.072	−3.021	−3.883
Rec_m^1	−0.426	−0.358	−0.423
Imc_m^1	−0.149	−0.176	−0.154

Table 2 NACA 64A010 CT8: Comparison of computational effort and storage requirements

Resource	FLM-SD.NS	FLM-NS
CPU time, h	1.1 $(3.7)^{SG}$[a]	12.3 $(19.3)^{SG}$
RAM, GByte	0.78 $(0.54)^{SG}$	0.22 $(0.13)^{SG}$

[a] $()^{SG}$ = computation with single-grid code.

established a bandwidth of values, it can be attested that the accuracy of FLM-SD.NS is well within their prediction limits.

Regarding the CT8 case, FLM-SD.NS surpasses FLM-NS by a factor off 11.7 in simulation speed (Table 2). The tradeoff for the enhanced efficiency lies in higher storage requirements, with FLM-SD.NS allocating more than triple the amount of working memory (RAM) as FLM-NS. Performing single-grid computations of the CT8 with FLM-SD.NS and FLM-NS yields a reduced CPU time ratio of 5.2 between the two methods. It becomes evident that the acceleration as a result of the multigrid technique does not transfer one to one between the small disturbance and time-accurate implementations, the scheme being more powerful in combination with the pseudo-steady-state solution process of FLM-SD.NS.

On basis of the CT8 case, a variation of the reduced frequency k_{red} is performed for further investigation of FLM-SD.NS performance. Ten distinct frequencies between $k_{\text{red}} \approx 0$ and $k_{\text{red}} = 2.0$ have been calculated with both FLM-SD.NS and FLM-NS. First harmonics of the unsteady lift and moment coefficient are plotted over the reduced frequency in Fig. 2. Real and imaginary parts of c_l^1 exhibit excellent conformity between the small disturbance and time-accurate method over the complete frequency spectrum. Larger deviations are apparent for c_m^1, with the real part being affected in the lower frequency range especially, as the difference in shock prediction widens. This behavior conforms with the previously discussed sensitivity of the integral coefficient c_m^1 to the deviations occuring in the shock region, whereas c_l^1 apparently is unaffected. As can be seen in Fig. 3, with decreasing k_{red} the CPU time ratio ζ between FLM-NS and FLM-SD.NS increases significantly. This is primarily attributed to the time-accurate solver's reduced performance at low frequencies, the convergence rate of FLM-SD.NS exhibiting far less variation over the frequency spectrum.

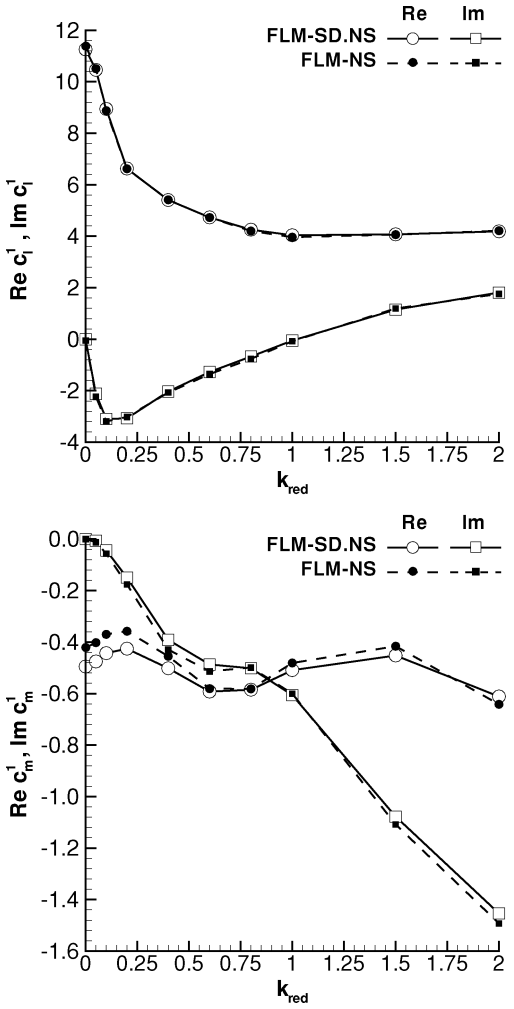

Fig. 2 Influence of the reduced frequency k_{red} on lift and moment coefficient prediction.

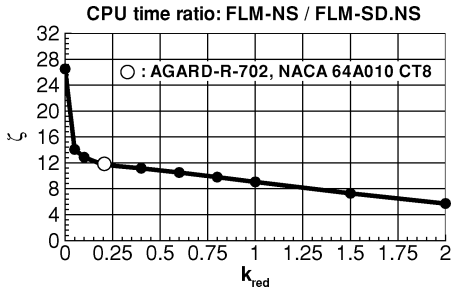

Fig. 3 Relative computational effort at distinct reduced frequencies k_{red}.

NLR 7301 Pitch Oscillations—Strong Shock Case

In stark contrast to the preceding airfoil, the supercritical NLR 7301 is defined by a blunt leading edge, a maximum relative thickness of 16.5%, and its rear loading character. Simulating the CT5 case from AGARD-R-702,[27] a pitch oscillation about an axis located at 40% chord length is conducted for the parameters given here: Ma_∞, 0.7; Re_∞, 2.1×10^6; $\bar{\alpha}$, 3.0 deg; $\hat{\alpha}$, 0.5 deg; k_{red}, 0.384; $\check{T}_\infty$, 288.15 K; c_r, 1.0; and l_{Re_∞}, 1.0. The reduced frequency of the simulation corresponds to a dimensional frequency of approximately 81 Hz. Because of the airfoil's geometric properties the computation becomes quite challenging, as the upper side shock is strong, with localized flow separation occuring in the post-shock as well as trailing edge region.

Reference and extremum grid employed in the FLM-SD.NS/FLM-NS simulation are equivalent to the ones used in the preceding test case, with the exception of increasing the cell quantity in contour normal direction to 128. As the off-body distance of the first grid line remains fixed at $1 \cdot 10^{-5} c_r$, the lower Reynolds number yields a $y^+ < 1.5$ across the airfoil. Again, the FLOWer simulation utilizes a single computational mesh equivalent to the FLM-SD.NS/FLM-NS reference grid, yet possesing a reduced off-body distance of $5 \cdot 10^{-6} c_r$. The enhanced resolution of the viscous sublayer as indicated by y^+ allows the use of the FLOWer implemented two-equation $k-\omega$ turbulence model.[30] Especially in the face of flow separation, it is deemed to provide better comparative results than the algebraic B/L model.[29] Obtaining a stable inviscid steady-state solution in the FLM-NS/FLM-SD.NS reference grid proved to be unachievable for this test case. This prompted the generation of a coarser grid with 192 cells in circumferential and 64 cells in the contour normal direction. Consequently, the NLR 7301 airfoil's discretization is decreased from 128 to 64 cells per side. In anticipation of the inviscid method predicting the upper-side shock farther downstream, the necessary increase in cell density was relocated accordingly. Having succesfully computed a stable

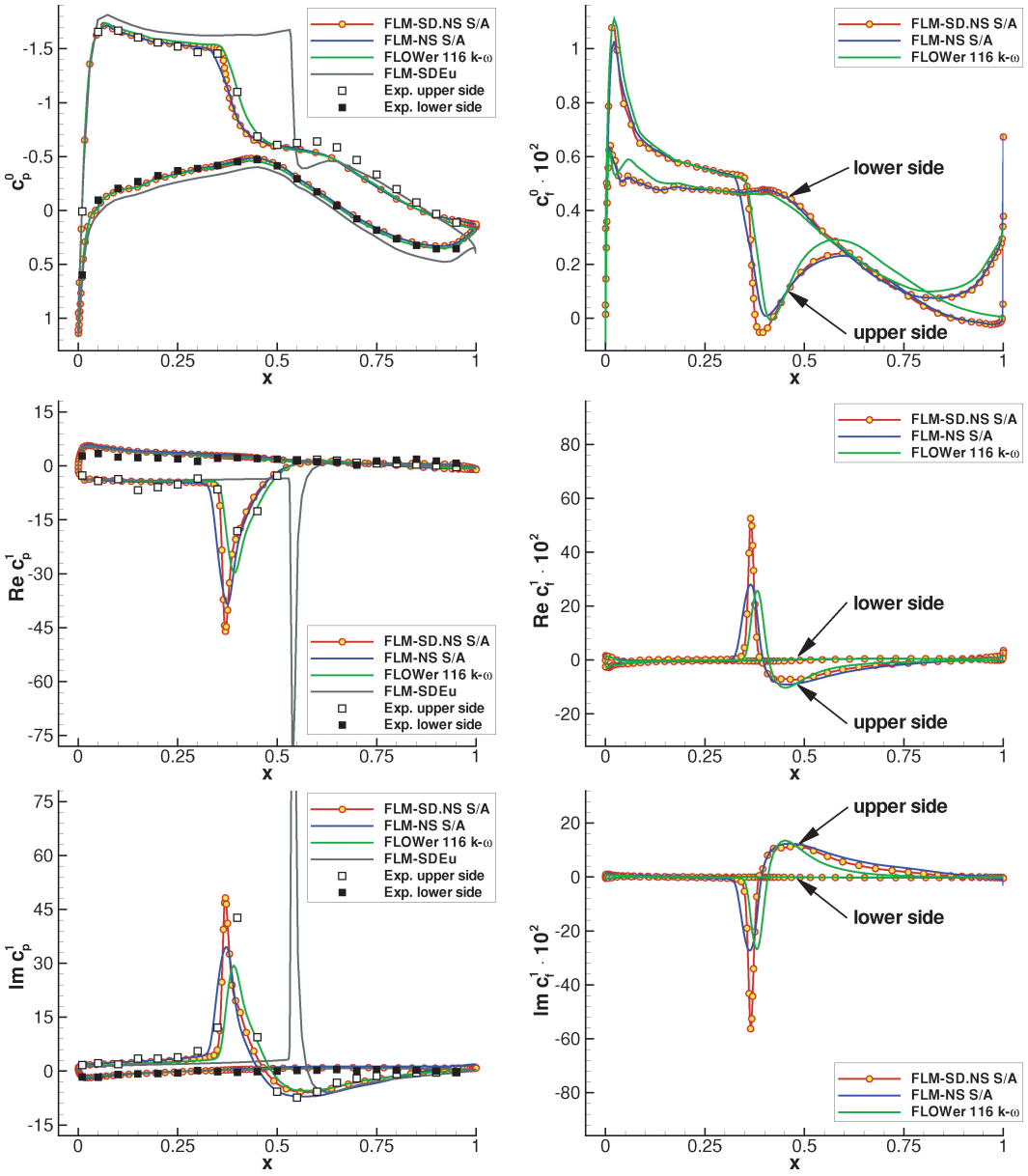

Fig. 4 Comparison of the pressure coefficient (c_p^0, c_p^1) and skin-friction coefficient (c_f^0, c_f^1) distributions for NLR 7301 CT5 ($Ma_\infty = 0.7, Re_\infty = 2.1 \cdot 10^6$, $\bar{\alpha} = 3.0$ deg, $\hat{\alpha} = 0.5$ deg, $k_{\text{red}} = 0.384$).

steady-state Euler solution, an inviscid extremum grid with equivalent properties is supplied for the FLM-SDEu calculation. Adapting the FLM.SD-NS solution scheme to this particular case, the already defined multigrid cycle is reduced to three levels, with the single pseudo time step now being limited to the intermediary grid level, while the abort criterium is modified to $5 \cdot 10^{-4}$. Equivalent settings are made for the time-accurate FLM-NS solution procedure, yet the number of computed oscillations as well as physical time intervals used in their discretization are unaltered. Results for FLM-SD.NS in comparision to FLM-NS, FLOWer, FLM-SDEu, and the experimental data are composited in Fig. 4.

Examining the zeroth harmonic of the pressure distribution, good conformity between the three viscous methods and the experiment is established. The characteristic suction plateau on the upper side is reproduced excellently, with minor variations apparent for shock initiation and extent. In this respect c_p^0 obtained from the unsteady FLOWer solution meets the experimental shock location best, with the FLM-SD.NS and FLM-NS prediction being slightly farther upstream. At the point of shock initiation, the c_p^0 distribution gained through FLM-NS exhibits a weaker gradient than the steady-state solution utilized by FLM-SD.NS. Even though all three viscous methods agree very well in their prediction of the rear-loading pressure distribution, the localized postshock increase in suction on the upper side as indicated by the experiment is not reproduced. The boundary layer's strong influence on shock formation becomes evident through the inviscid solution, where the shock is situated 20% farther downstream in comparison to the viscous prediction.

Adhering directly to the airfoil's upper contour, shock resolution is crisp with a very strong gradient and the typical overextended recompression. Subsequently, the inviscid progression merges into the pressure recovery curve computed by the viscous methods before deviating again toward the trailing edge. Conformity in the zeroth harmonic of the skin-friction distribution is also quite well. In shock vicinity and toward the upper-side trailing edge, the steady-state solution exhibits negative c_f^0 values, indicating local regions of flow separation. Neither unsteady distribution computed by FLM-NS and FLOWer shows postshock flow reversal in the zeroth harmonic, yet FLM-NS agrees excellently with FLM-SD.NS toward the trailing edge. The $k-\omega$ turbulence model[30] employed by FLOWer produces consistently positive and higher values for c_f^0 beyond the shock. Real and imaginary parts of the first harmonic pressure and skin-friction distributions (c_p^1, c_f^1) are clearly dominated by the upper-side peak

Table 3 NLR 7301 CT5: Comparison of the computed global coefficients

Coefficient	FLM-SD.NS	FLM-NS	FLOWer
Rec_l^1	5.712	6.461	5.349
Imc_l^1	−1.311	−0.864	−1.244
Rec_m^1	−0.321	−0.414	−0.272
Imc_m^1	−0.490	−0.716	−0.402

indicating the extent of the shock's motion in course of the pitch oscillation. Agreement of FLM-SD.NS to the two time-accurate viscous methods and the experimental data is again quite well for the critical shock region, with the peaks displaying the typical narrower progression with a larger absolute maximum value. However, the occurring differences are far greater than those witnessed in the NACA 64A010 CT8 case, correlating to the deviations already observed in the zeroth harmonics. Further investigating this behavior, Fourier analysis of the unsteady FLM-NS and FLOWer data beyond the first harmonic reveals the presence of higher harmonics in the shock region, contributing in a nonneglectable manner to the time-dependent evolution of pressure and skin friction. As FLM-SD.NS is based on the strict decomposition of the unsteady flow into a mean and linear perturbation part, the dynamically nonlinear influences of these higher harmonics naturally are unaccounted for. Outside the region of shock influence, conformity between FLM-SD.NS, FLM-NS, FLOWer, and the experimental data is excellent. In these areas the convective properties of the flow clearly dominate, as put into evidence by the c_p^1 distribution provided by FLM-SDEu. Yet, the predicted location of the pressure peak for both Rec_p^1 and Imc_p^1 is distinctly off, obviously correlating to the inviscid c_p^0 shock position at 55% chord length. Because of the shock's strong gradient, FLM-SDEu computes a highly defined c_p^1 peak with an absolute maximum value far exceeding the other data. Unsteadiness in the near-wall region as reflected by c_f^1 is apparently limited to the shock/postshock region, with skin friction on the lower side being seemingly unaffected by the motion. Considering c_f^1 in respect to c_f^0 establishes that postshock flow separation, and reattachment is present throughout the complete oscillation.

Overall the NLR 7301 CT5 case is computed in good quality by FLM-SD.NS, with definite deviations being observed in the shock/postshock region for the local distributions's first harmonic. Having already discussed the global coefficients susceptibility to such differences and given the presence of contributing higher harmonics in the time-accurate solutions, the assesment of c_l^1 and c_m^1 prediction ability becomes rather difficult. Even though the FLM-SD.NS values are well within the ranges established by the first harmonics gained through FLM-NS and FLOWer (Table 3), especially the bandwidth for c_m^1 (reference axis at 25% c_r) is too large to ascertain accuracy. However, the general tendency of FLM-SD.NS being closer to FLOWer in its values can be established. The CPU time ratio between FLM-NS and FLM-SD.NS is approximately three, with FLM-SD.NS requiring 3.2 h for the computation.

Grid Sensitivity

As indicated earlier, the solution of the small disturbance Navier–Stokes equations develops in response to the source term $\hat{\boldsymbol{S}}^{(2)}$, which contains the products between pertubation metrics and mean flow values. Consequently, the spatial discretization's influence on the FLM-SD.NS prediction is primarily an issue of quality in regard to the supplied steady-state solution. Concerning the transonic flow regime, good resolution of any occurring discontinuity becomes imperative because the FLM-NS computed location and intensity of the shock directly affects the FLM-SD.NS first harmonic. With this in mind, the reference grids respectively employed in NACA 64A010 CT8 and NLR 7301 CT5 simulations were optimized for capturing the steady-state shock as best as possible. Investigating the FLM-SD.NS sensitivity to the spatial discretization, a coarser reference grid was generated for each NACA 64A010 and NLR 7301 airfoil by means of eliminating every second initial grid vertex. Hence, the global number of cells discretizing the physical domain is reduced by 75%. Comparing the steady-state pressure distributions computed on the coarser reference grids, a slightly weaker shock gradient is observed for the NACA 64A010 case, being the only noticeable deviation. On the other hand the NLR 7301 case exhibits a shock displacement by 6% chord length toward the leading edge, a weaker gradient also being evident. Setting up the FLM-SD.NS calculation, coarser extremum grids are generated according to the preceding procedure. For the NACA 64A010 case the weaker shock gradient seen in the steady-state pressure distribution leads to a decrease of the absolute pressure peak value by approximately 25% in the FLM-SD.NS first harmonic, while the extent of the peak region becomes marginally wider. This correlation between c_p^0 and c_p^1 is characteristic for FLM-SD.NS, minor deviations in the steady-state shock locally affecting the order of magnitude smaller first harmonic in a distinguishable manner. For the NLR7301 case achieving a stable FLM-SD.NS solution on the coarser grids proved to be futile, the spatial discretization toward the trailing edge being insufficient to adequately resolve the perturbation of the eddy viscosity.

Conclusions

In context of the external flow problem associated with aircraft aerodynamics, it was the goal of this study to provide the aeroelastician with an efficient tool for predicting unsteady airloads, realizing not only high-quality resolution of flow discontinuities, but also accounting for viscous effects. On the basis of the small disturbance Navier–Stokes equations, such a means has been devised in form of the computational method FLM-SD.NS. Incorporating an appropriate small disturbance formulation of the Spalart–Allmaras one-equation tubulence model allowed for the treatment of high-Reynolds-number flows. The validity of this approach was demonstrated for two distinct airfoils performing harmonic pitch oscillations in transonic freestream, thus inducing a flowfield characterized by unsteady shock/boundary-layer interaction of varying strength. Overall good agreement in the results between the small disturbance and the time-accurate methods as well as the experimental data was observed. Reductions in computational time up to an order of magnitude are ascertained. Having laid the theoretical and numerical groundwork, an extension to three dimensions is straightforward and has been completed in the meantime. Validation of the small disturbance Navier–Stokes method with a delta wing performing harmonic pitch oscillations is being conducted, with results showing promise in respect to solution quality and efficiency.

References

[1]Hall, K. C., and Crawley, E. F., "Calculation of Unsteady Flows in Turbomachinery Using the Linearized Euler Equations," *AIAA Journal*, Vol. 27, No. 6, 1989, pp. 777–787.

[2]Lindquist, D. R., and Giles, M. B., "Validity of Linearized Unsteady Euler Equations with Shock Capturing," *AIAA Journal*, Vol. 32, No. 1, 1994, pp. 46–53.

[3]Kreiselmaier, E., "Berechnung Instationärer Tragflügelumströmungen auf der Basis der Zeitlinearisierten Eulergleichungen," Ph.D. Dissertation, Inst. for Fluid Mechanics, Technische Univ. München, Garching, Germany, July 1998.

[4]Kreiselmaier, E., and Laschka, B., "Small Disturbance Euler Equations: Efficient and Accurate Tool for Unsteady Load Predictions," *Journal of Aircraft*, Vol. 37, No. 5, 2000, pp. 770–778.

[5]Sickmüller, U., Pechloff, A., Weishäupl, C., and Laschka, B., "Aerodynamische Untersuchungen eines Deltaflügels bei Verschiedenen Eigenformen Mittels eines Euler-Verfahrens bei Kleinen Störungen," Deutscher Luft- und Raumfahrtkongress, DGLR Paper 2001-065, Hamburg, Germany, Sept. 2001.

[6]Weishäupl, C., and Laschka, B., "Small Disturbance Euler-Simulations for Unsteady Flows of a Delta Wing due to Harmonic Oscillations," *Journal of Aircraft*, Vol. 41, No. 4, 2004, pp. 782–789.

[7]Allen, A., Weishäupl, C., and Laschka, B., "Flap Efficiency of a Delta Wing with an External Store Using an Euler Code for Small Disturbances," *New Results in Numerical and Experimental Fluid Mechanics IV: Contributions to the 13th STAB-DGLR-Symposium, Munich, Germany, 2002*, edited by C. Breitsamter, B. Laschka, H.-J. Heinemann, and R. Hilbig, Notes on Numerical Fluid Mechanics and Multidisciplinary Design, Vol. 87, Springer-Verlag, Berlin, 2004, pp. 116–123.

[8]Clark, W. S., and Hall, K. C., "A Time-Linearized Navier–Stokes Analysis of Stall Flutter," *Journal of Turbomachinery*, Vol. 122, No. 3, 2000, pp. 467–476.

[9]Petrie-Repar, P., "Development of an Efficient Linearised Navier–Stokes Flow Solver for Turbomachinery Applications," *New Results in Numerical and Experimental Fluid Mechanics IV: Contributions to the 13th STAB-DGLR-Symposium, Munich, Germany, 2002*, edited by C. Breitsamter, B. Laschka, H.-J. Heinemann, and R. Hilbig, Notes on Numerical Fluid Mechanics and Multidisciplinary Design, Vol. 87, Springer-Verlag, Berlin, 2004, pp. 286–293.

[10]Laschka, B., "Unsteady Flows—Fundamentals and Applications," *Unsteady Aerodynamics—Fundamentals and Applications to Aircraft Dynamics*, AGARD 386, 1985, pp. 1-1–1-21.

[11]Telionis, P. D., *Unsteady Viscous Flows*, Springer-Verlag, New York, 1981, pp. 224–228.

[12]Morkovin, M. V., "Effects of Compressibility on Turbulent Flows," *Mécanique de la Turbulence*, edited by A. Favre, Gordon and Breach, New York, 1962, pp. 367–380.

[13]Acharya, M., "Measurements and Predictions of a Fully Developed Turbulent Channel Flow with Imposed Controlled Oscillations," Ph.D. Dissertation, Dept. of Mechanical Engineering, Stanford Univ., Stanford, CA, May 1975.

[14]Norris, H. L., "Turbulent Channel Flow with a Moving Wavy Boundary," Ph.D. Dissertation, Dept. of Mechanical Engineering, Stanford Univ., Stanford, CA, May 1975.

[15]Pechloff, A., "Triple Decomposition of the Two-Dimensional Navier–Stokes Equations in Cartesian Coordinates and Linearization for Small Disturbances," Inst. for Fluid Mechanics, Technische Univ. München, Rept. TUM-FLM-2001/4, Garching, Germany, March 2001.

[16]Spalart, P. R., and Allmaras, S. R., "A One-Equation Turbulence Model for Aerodynamic Flows," AIAA Paper 92-0439, Jan. 1992.

[17]Pechloff, A., Iatrou, M., Weishäupl, C., and Laschka, B., "The Small Disturbance Navier–Stokes Equations: Development of an Efficient Method for Calculating Unsteady Air Loads," *New Results in Numerical and Experimental Fluid Mechanics IV: Contributions to the 13th STAB-DGLR-Symposium, Munich, Germany, 2002*, edited by C. Breitsamter, B. Laschka, H.-J. Heinemann, and R. Hilbig, Notes on Numerical Fluid Mechanics and Multidisciplinary Design, Vol. 87, Springer-Verlag, Berlin, 2004, pp. 278–285.

[18]Chakravarthy, S. R., "High Resolution Upwind Formulations for the Navier–Stokes Equations," von Kármán Inst. Lecture Series on Computational Fluid Dynamics, VKI 1988-05, von Kármán Inst., Brussels, 1988, pp. 1–105.

[19]Iatrou, M., Weishäupl, C., and Laschka, B., "Entwicklung eines Instationären Navier–Stokes-Verfahrens bei Kleinen Störungen für Aeroelastische Problemstellungen," Inst. for Fluid Mechanics, Technische Univ. München, Rept. TUM-FLM-2002/9, Garching, Germany, April 2002.

[20]Jameson, A., and Turkel, E. "Implicit Schemes and LU-Decompositions," *Mathematics of Computation*, Vol. 37, No. 156, 1981, pp. 385–397.

[21]Blazek, J., "Investigations of the Implicit LU-SSOR Scheme," Inst. for Design Aerodynamics, German Aerospace Research Center (DLR), Rept. DLR-FB 93-51, Braunschweig, Germany, July 1993.

[22]Blazek, J., "A Multigrid LU-SSOR Scheme for the Solution of Hypersonic Flow Problems," AIAA Paper 94-0062, Jan. 1994.

[23]Pechloff, A., "An Implicit Method for Solving the Small Disturbance Navier–Stokes Equations," Inst. for Fluid Mechanics, Technische Univ. München, Rept. TUM-FLM-2002/21, Garching, Germany, Sept. 2002.

[24]Cvrlje, T., Breitsamter, C., Weishäupl, C., and Laschka, B., "Euler and Navier–Stokes Simulation of Two Stage Hypersonic Vehicle Longitudinal Motions," *Journal of Spacecraft and Rockets*, Vol. 37. No. 2, 2000, pp. 242–251.

[25]Iatrou, M., Weishäupl, C., and Laschka, B., "Entwicklung eines Instationären Navier–Stokes-Verfahrens bei Kleinen Störungen für Aeroelastische Problemstellungen," Aerodynamics Division, Inst. for Fluidmechanics, Technische Univ. München, Rept. TUM-FLM-2003/27, Garching, Germany, Oct. 2003.

[26]Davis, S. S., "NACA 64A010 (NASA Ames Model) Oscillatory Pitching," *Compendium of Unsteady Aerodynamic Measurements*, AGARD-R-702, 1982, pp. 2-1–2-22.

[27]Zwaan, R. J., "NLR 7301 Supercritical Airfoil Oscillatory Pitching and Oscillating Flap," *Compendium of Unsteady Aerodynamic Measurements*, AGARD-R-702, 1982, pp. 4-1–4-25.

[28]Kroll, N., *FLOWer Version 116 Installation and User Handbook*, Inst. for Design Aerodynamics, German Aerospace Research Center (DLR), Braunschweig, Germany, 2001.

[29]Baldwin, B. S., and Lomax, H., "Thin Layer Approximation and Algebraic Model for Separated Turbulent Flows," AIAA Paper 78-257, Jan. 1978.

[30]Wilcox, D. C., "Reassessment of the Scale-Determing Equation for Advanced Turbulence Models," *AIAA Journal*, Vol. 26, No. 11, 1988, pp. 1299–1310.